Estimating velocity distribution and flood discharge at river bridges using the entropy theory. Insights from Computational Fluid Dynamics flow fields

Farhad Bahmanpouri[1†], Tommaso Lazzarin[2†], Silvia Barbetta[1], Tommaso Moramarco[1], Daniele P. Viero[2]

[1]Research Institute for Geo-Hydrological Protection, National Research Council (CNR), Perugia, 06128, Italy
[2]Department of Civil, Environmental and Architectural Engineering, University of Padova, 35131, Italy

[†] F.B. and T.L. equally contributed to the study.

Correspondence to: Daniele P. Viero (daniele.viero@unipd.it)

Abstract. Estimating the flow velocity and discharge in rivers is of particular interest for monitoring, modelling, and research purposes. Instruments for measuring water level and surface velocity are generally mounted on bridge decks, and this poses a challenge because the bridge structure (e.g., piers and abutments) can lead to perturbated flow fields. The current research aims to investigate the applicability of the entropy theory to estimate the velocity distribution and the discharge in the vicinity of river bridges. To this purpose, a Computational Fluid Dynamics (CFD) model is used to obtain three-dimensional flow fields along a stretch of the Paglia River (central Italy), where a historical multi-arch bridge strongly affects flood flows. The input data for the entropy model include the cross-sectional bathymetry and the surface velocity provided by the numerical simulations. A total of 12 samples, including three different flow conditions for four cross-sections, one upstream and three downstream of the bridge, are considered. It is found that the entropy model can be reliably applied upstream of the bridge, also when forced with a single (i.e., the maximum) value of the surface velocity, with errors on total discharge below 13% in the considered case. On the contrary, downstream of the bridge, the wakes generated by the bridge piers strongly affect the velocity distribution, both in the spanwise and in the vertical directions, and for very long distances. Here, notwithstanding the complex and multimodal spanwise distribution of flow velocity, the entropy model estimates the discharge with error lower than 8% if forced with the river-wide distribution of the surface velocity. The present study has important implications for the optimal positioning of sensors and ~~suggest~~suggests the potential of using CFD modelling and entropy theory jointly to foster the knowledge of river systems.

1 Introduction

Velocity and discharge measurements in rivers are fundamental for monitoring, modelling, and research purposes (Depetris, 2021; Di Baldassarre and Montanari, 2009; Dottori et al., 2013; Gore and Banning, 2017; Herschy, 2009). Unfortunately, measuring river discharge can be very challenging due to different reasons, for example in the case of intermittent rivers typical of semi-arid regions, of flash floods in mountain areas, of flood flows involving wide floodplains, of freshwater flows affected

30   by saline tidal intrusions in estuaries, etc. While monitoring river discharge on the ground has definite advantages (Fekete et al., 2012), the use of traditional methods such as current meters and ADCPs is generally expensive, time-consuming, and risky for operators, mainly during severe flow conditions, and such methods are not ~~feasible~~applicable in remote and inaccessible locations.

Different techniques can be used to measure the surface velocity, also during severe flood conditions, including Large-Scale
35   Particle Image Velocimetry (LSPIV) (Eltner et al., 2020; Jodeau et al., 2008; Le Coz et al., 2010; Muste et al., 2011, 2014), Space-Time Image Velocimetry (STIV) (Fujita et al., 2007, 2019), Infrared Quantitative Image Velocimetry (Schweitzer and Cowen, 2021), and other methods based on the use of either terrestrial or Unmanned Aerial System sensors (Bandini et al., 2020, 2021; Herschy, 2009).

Indirect methods have then been proposed to estimate the flow discharge using this kind of remote sensed data (Bogning et
40   al., 2018; Fekete and Vörösmarty, 2002; Spada et al., 2017; Vandaele et al., 2023; Zhang et al., 2019). The flowrate is generally obtained by applying suitable velocity coefficients to estimate the depth-averaged velocity or by integration of a hypothetical flow velocity distribution in the cross-sectional area. The key point is thus estimating the depth-averaged velocity, or its full cross-sectional distribution, starting from surface velocity data, a process whose reliability depends on the (un)evenness of the actual velocity distribution.

45   In natural rivers with large cross-sections, the streamwise velocity typically shows a logarithmic vertical distribution, mainly determined by the bottom roughness. According to field data, the maximum velocity is found just below the free surface and gradually decreases towards the bed (Franca et al., 2008; Guo, 2014). However, plenty of factors contributes ~~in~~to making the velocity distribution irregular. For instance, channel bends and deformed bathymetry produce large-scale secondary currents (Constantinescu et al., 2011; Lazzarin and Viero, 2023; Yang et al., 2012), and the presence of banks and of discontinuities of
50   bed elevation in the spanwise directions can generate secondary currents of the second kind because of turbulence heterogeneity (Nikora and Roy, 2011; Proust and Nikora, 2020), which all increase the three-dimensionality of the flow field and alter the vertical and spanwise distribution of the flow velocity.

The presence of in-stream structures, such as bridges characterized by the presence of piers and/or of lateral abutments, can induce further alterations on the flow field (Laursen, 1960, 1963), producing complex and rapidly varying flow patterns, with
55   the formation of strong three dimensional flow structures (Ataie-Ashtiani and Aslani-Kordkandi, 2012; Chang et al., 2013; Salaheldin et al., 2004). Secondary currents in the cross-section transport low momentum fluid from lateral region to the center of the channel, and high-momentum fluids from the free surface toward the bed (Bonakdari et al., 2008; Nezu and Nakagawa, 1993; Yang et al., 2004). ~~This creates systems~~Systems of vortices with horizontal (horseshoe vortex) or vertical axes (wake vortex) ~~that in turn~~ modify the velocity distribution (Kirkil and Constantinescu, 2015; Sumer et al., 1997). The wakes generated
60   by in-stream obstacles and contractions can produce uneven spatial distributions of the water surface elevations close to the bridge, and can propagate downstream of bridges thus altering the cross-sectional velocity distribution for quite long distances (Briaud et al., 2009; Yang et al., 2021). Furthermore, because of particular bridge shape (e.g., arch-piers) and of irregular cross-sections (e.g., compound sections), the flow field may show a marked dependence on the water depth and the flowrate.

Even though the above factors complicate inferring the cross-sectional velocity distribution (and thus the flow discharge) based

65   on surface velocity data in the vicinity of in-stream structures, it has to be observed that measuring instruments such as hydrometers, as well as radar sensors or cameras for estimating the surface velocity, are often mounted on bridge decks for convenience reasons. Notwithstanding the recommendation of installing height gage at the upstream side of bridges (Meals and Dressing, 2008), measuring instruments are often located downstream of bridges, where the flow field unevenness is expected to further complicate the discharge estimation (Kästner et al., 2018). Besides the measurement of the flow discharge,

70   the knowledge of flow field nearby bridges has additional practical implications; the flow velocity is the dominant parameter to study the local scour at a bridge pier, which may result in being responsible for the bridge collapse in some extreme conditions (Barbetta et al., 2017; Federico et al., 2003; Lu et al., 2022). The formation of scours at piers and abutments can be attributed to a significant extent to the flow patterns produced at their immediate vicinity, such as the flow contraction and the large-scale turbulent structures (Cheng et al., 2018; Khosronejad et al., 2012).

75   One of the most promising methods to estimate the cross-sectional velocity distribution from joint measures of water level and surface velocity is based on the entropy concept. Researchers have widely applied this concept to predict velocity distributions, the flow discharge, and other relevant parameters in open channels (Bahmanpouri et al., 2022b; Bonakdari et al., 2015; Chahrour et al., 2021; Chiu, 1989; Chiu et al., 2005; Chiu and Said, 1995; Ebtehaj et al., 2018; Moramarco et al., 2019; Moramarco and Singh, 2010; Singh et al., 2017; Sterling and Knight, 2002; Termini and Moramarco, 2017; Vyas et al., 2021).

80   Recent applications of the entropic velocity distribution include the case of large meandering channels (Termini and Moramarco, 2020), the estimation of the depth-averaged velocity as a function of the aspect ratio (Abdolvandi et al., 2021), the confluence of the large Negro and Solimões rivers (Bahmanpouri et al. 2022a), and the regularizing of the entropy parameter (Ammari et al., 2022). One advantage of the entropy approach is providing the complete cross-sectional distribution of velocity, whereas other indirect methods for estimating flow discharge only compute the depth-averaged value from the

85   surface velocities at subsections using a fixed reduction coefficient (e.g., Le Coz et al., 2010). Previous studies demonstrated the accuracy of the entropy method referring to undisturbed flow conditions, and also to cases like confluences or low curvature bends characterized by large-scale three-dimensional effects and secondary currents.

The present research is meant to investigate the predictive ability of the entropy theory in estimating the velocity distribution, and hence the streamflow discharge, in the case of complex flow fields generated by the presence of bridges. It is of particular

90   relevance because, as already noted, water levels and free-surface velocities are often measured by instruments mounted on bridges, where the flow-structure interaction can significantly disturb the flow field.

Considering that measuring the cross-sectional velocity distribution in the vicinity of bridges is practically unfeasible in flood conditions, in the present study a three-dimensional Computational Fluid Dynamics (3D-CFD) model is used to obtain physics-based and high-resolution descriptions of the real flow field, for a sufficiently long river segment and for different values of

95   the flow discharge. The CFD-computed surface velocity (either a single value or its river-wide distribution) ~~are~~is used as input for the entropy model, thus simulating the availability of suitable remote sense instruments. Then, the cross-sectional velocity distributions provided by the entropic model are benchmarked against those computed by the CFD model, which allows

assessing the reliability of the entropy model. The exercise is repeated for different cross-sections, both upstream and downstream of the bridge, to investigate the pros and cons of different locations where estimating the discharge, thus to provide

100 applicative guidelines. A reach of the Paglia River, in the central Italy, is chosen as a relevant case study; here, a level gauge and a radar sensor for measuring the surface velocity are mounted on a historical multi-arch bridge, which produces strong flow-structure interactions.

The present analysis allows providing guidelines for the proper application of the entropy theory and the optimal choice and positioning of measuring instruments, aimed at the reliable estimation of flow discharge in the vicinity of river bridges.
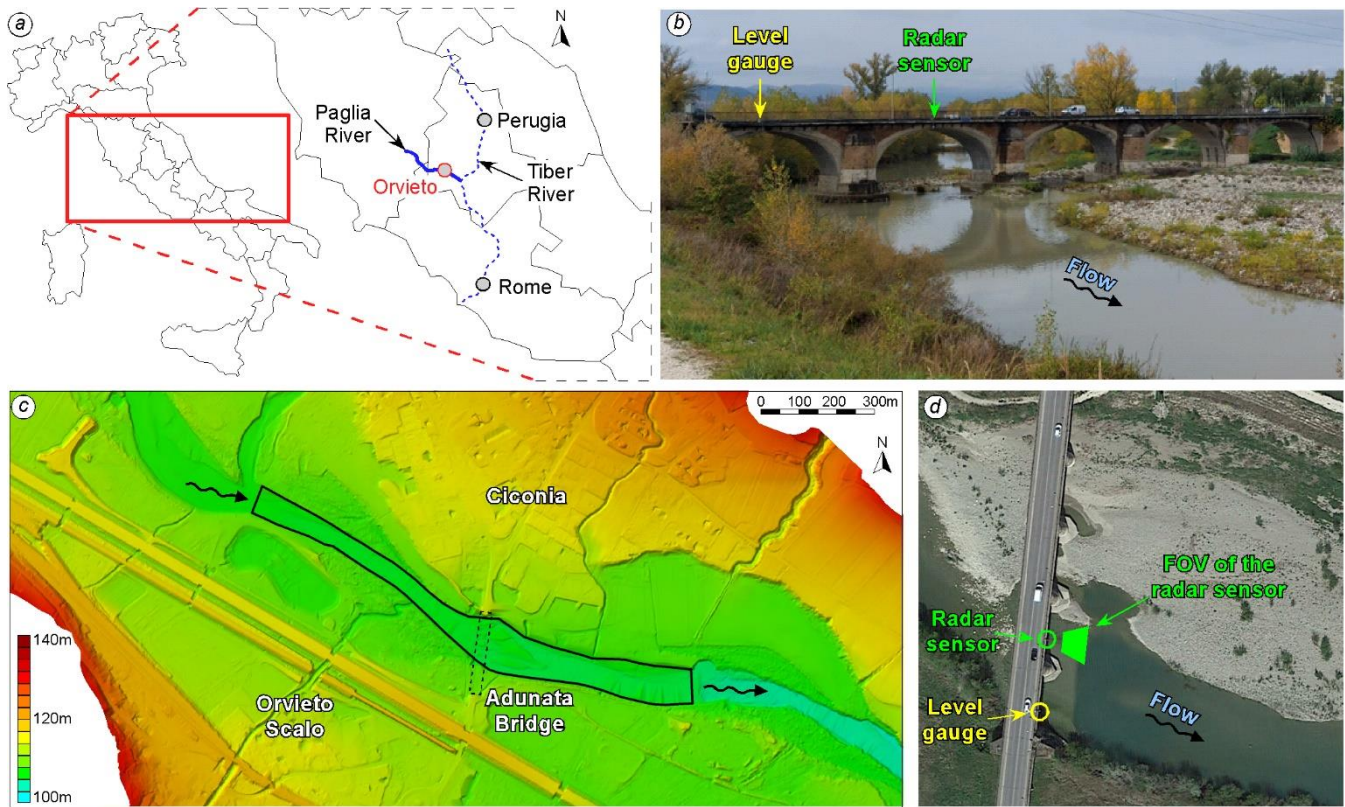
Figure 1. a) Location of the field site; b) downstream view of the Adunata bridge on the Paglia River during normal flow condition (11.11.2021); c) Digital Terrain Model (DTM) nearby the Adunata bridge (dotted line), with the domain of the 3D CFD model (black line); d) location of the level gauge and of the radar sensor with the field of view (FOV) on aerial image (© Google Earth).

2 Material and Methods

110 ### 2.1 Field Site

The Paglia River, in the central part of Italy (Figure 1a), is a tributary of Tiber River, subjected to severe flooding and high sediment transport. The reach of interest is across the Adunata bridge (Figure 1b), near the town of Orvieto, where the Paglia

River subtends a basin area of about 1'200 km². Here, the average discharge is of 10 m³/s; however, flood discharge can reach estimated values of up to 2'500 m³/s.

115 The Adunata bridge connects the settlements of Orvieto Scalo and Ciconia, as part of the Italian State Road n.71 (Figure 1c). It is a masonry multi-arch bridge, with 5 arches ending at four piers on the river bed. On the right-hand side, an abutment sustains the bridge and separates it from the floodplain; on the left-hand side, the bridge deck is supported by the main levee. Close to the bottom, the piers have a roughly elliptical shape with the major axis, aligned with the flow, 15 m long, and the minor axis, orthogonal to the flow, 5.7 m wide. At the bottom, each pier is sustained by an elliptical plinth whose profile is

120 2.0 m larger than the pier. The center-distance between the piers is 23.2 m. The piers width increases approaching the deck because of the arches; the deck width is approximatively 10 m.

The main thread of the flow is at the right-hand side of the river, and a large depositional area forms on the left-hand side just downstream of the bridge (Figure 1b). The main channel axis is characterized by a significant curvature, bending to the left at the bridge section (Figure 1c).

125 ## 2.2 Available Data

In the downstream side of the Adunata Bridge, a water level gauge is placed at the center of the first arch, and a radar sensor for measuring the water surface velocity is located at the second arch (Figure 1d). The field of view (FOV) of the radar sensor is also shown in Figure 1d. The time resolution of both the sensors is 10 min.

In addition, a number of flowrate measures and cross-sectional velocity distributions are provided by the Umbria Region

130 Hydrological Service. The flowrate data were collected using a current meter a few tens of meters downstream of the Adunata Bridge, by wading in the period 2009-2011 (flowrate ranging between 3.3 and 14.3 m³/s), and from the bridge in the period 1995-2010 (flowrate ranging between 16.8 and 147 m³/s); additional flowrate data were collected using an Acoustic-Doppler Current Profiler (ADCP) some hundreds of meters upstream of the bridge in the period 2014-2019 (flowrate ranging between 0.37 and 45 m³/s). The official rating curve for the Adunata Bridge, provided by ARPA Lazio, is based on these measures.

135 As detailed in the following sections, the rating curve derived from current meter and ADCP data, the water levels, and the free-surface velocity data collected by the sensors mounted on the Adunata bridge, were used to validate the hydrodynamic numerical models (Sect. 2.3 and Appendix A). The cross-sectional velocity distributions measured with the current meter just downstream of the bridge were used to further assess the spatial variability of the entropy-based velocity distributions, as detailed in Sect. 3.1.

140 ## 2.3 Numerical Model

The commercial CFD software STAR-CCM+ (Siemens) was used for the numerical simulations. It implements the Finite Volume method to compute the flow field on unstructured, Cartesian computational grids. The software has been used and validated in several applications for flow over deformed bathymetry in presence of obstacles (Chang et al., 2013; Kirkil et al., 2009; Lazzarin et al., 2023c) and channel bends (Constantinescu et al., 2011, 2013; Koken et al., 2013). In the present

application, the two-phase Volume of Fluid (VoF) method was used to distinguish water and air in the computational domain (Hirt and Nichols, 1981). This method was shown to well capture the water surface in complex open channel flows (Horna-Munoz and Constantinescu, 2018; Lazzarin et al., 2023b; Li and Zhang, 2022; Luo et al., 2018; Yoshimura and Fujita, 2020). In the used setup, the model solved the Reynolds-Averaged Navier-Stokes (RANS) equations, in which the stress tensor in the momentum equations is related to the mean flow quantities by adopting the Bousinnesq approximation. The eddy viscosity, μ_T, was determined by solving transport equations for the turbulent kinetic energy, k, and dissipation rate, ε, according to the realizable k-ε turbulence model (Shih et al., 1995), which was shown to provide reliable predictions for large-scale complex flows in natural rivers (e.g., Horna-Munoz and Constantinescu, 2018).

The simulations were advanced in time with an implicit, 1st order discretization, until reaching steady state conditions. The computational domain reproduced a ~1,100 m long reach of the Paglia River (Figure 1c), centered at the Adunata bridge. The average size of the grid elements was of 1.0 m. Starting 100 m upstream of the bridge and up to 300 m downstream of the bridge, the grid was refined using elements with average length 0.5 m. To well capture the near-wall boundary layer, a prism layer refinement with three layers was used to reduce the wall-normal thickness of the grid cells close to solid boundaries (i.e., the riverbed and bridge structure). The final computational grid was made of ~4 million elements.

A rough-wall, no-slip condition was imposed at the solid boundaries by means of a wall function (roughness height of 0.1 m at the bottom, and of 0.01 m at the bridge surfaces). The upper boundary of the computational grid was treated as a symmetry plane (i.e., slip-condition) for the air-flow. The water elevation at the outlet (i.e., downstream section) was kept fixed in time by imposing a suitable hydrostatic-pressure distribution. The value of the downstream level, for each of the simulated scenarios, was derived from an auxiliary two-dimensional (2D), depth-averaged hydrodynamic model calibrated on available data; the 2DEF model has been used to this purpose (see Appendix A for details on the model and its calibration/verification). A constant-in-time, logarithmic velocity distribution was imposed as upstream boundary condition for the water fraction. For the air fraction (upper part of the numerical domain), zero velocity and zero pressure were imposed at the inlet and at the outlet, respectively.

The 3D-CFD model was validated by comparing the surface velocity computed by the model with those measured by the radar sensor located downstream of the bridge (see the yellow bullets in Fig. A2c,d, in the Appendix A).

2.4 Flood events considered in the study

Three different steady flow conditions have been simulated with the 3D-CFD model STAR-CCM+, which correspond to the peak flow conditions of flood events occurred in 2012, 2019, and 2022 as provided by the rating curve for the Adunata Bridge (Table 1). In all the three flow conditions, water flowed in the main channel and over the sediment bars that are dry in the low flow condition of Figure 1b,d. During the most severe flood of 2012, water flowed on the floodplains adjacent to the main river and caused the incipient pressurization of flow below the bridge arches. The preliminary simulation carried out with the 2DEF depth-averaged model showed that, at the peak of the 2012 flood event, 700 m³/s flowed through the floodplain, overflowing the bridge access roads, and 1800 m³/s flowed within the main channel; this last value was used in the 3D-CFD

simulation, which considered only the main channel of the river. The flood events of 2019 and 2022, although being quite ordinary, were the largest floods occurred after the installation of the radar sensor for the surface velocity data (surface velocity data were not available for the 2012 flood).

Event	Discharge [m³/s]	Return period (years)
2012	1800 (2500)	200
2019	450	2
2022	160	1

Table 1. Simulations performed in the present work. The value in brackets indicate the total discharge considering also the flow over floodplains, not considered in the 3D simulations.

2.5 Entropy theory

The Entropy theory deals with physical systems that may have a large number of states from a probabilistic point of view. The concept of entropy is used for statistical inference, to determine a probability distribution function when the available information is limited to some average quantities, defined as constraints such as mean and variance. For the application of entropy to streamflow measurements, the pioneer was Chiu (1987), who developed a probabilistic formulation of the cross-sectional velocity distribution in open channels, in which the expected value of the point velocity is determined by applying the maximum entropy principle (Chiu, 1987, 1988, 1989). Using this probabilistic formulation, the velocity distribution is given analytically as a function of the cross-sectional geometry, of the dimensionless entropy parameter, M, and possibly of the depth at which the maximum velocity occurs (the so-called dip, h). There is a one-to-one correspondence between M and the ratio of mean to maximum velocity in the cross-section, which is defined as the entropic function, $\phi(M)$ (Chiu, 1991). In general, for a given river site, the magnitude of M and, in turn, of $\phi(M)$, mainly depend on hydraulic parameters such as roughness and hydraulic radius, whereas they are poorly affected by the flow discharge (Chiu and Murray, 1992; Moramarco and Singh, 2010). Moreover, $\phi(M)$ is consistently found to be nearly constant at different cross-sections through gauged river sites for different flow conditions (Moramarco and Singh, 2010; Ammari et al., 2022). This is because the value of $\phi(M)$ is associated with geometric and hydraulic characteristics that tend to vary smoothly within a river system (Ammari et al., 2022). The estimation of cross-sectional velocity distribution, $U(x,y)$, developed by Chiu (1989), was later simplified by Moramarco et al. (2004). Using this approach, one can divide the wet cross-sectional area into N_v verticals and determine the entropy-based velocity profile along each vertical as

$$U(x_i, y) = \frac{U_{max}(x_i)}{M} \ln\left[1 + (e^M - 1)\frac{y}{D(x_i) - h(x_i)}\exp\left(1 - \frac{y}{D(x_i) - h(x_i)}\right)\right] \quad i = 1 \dots N_v \tag{1}$$

where U is the time-averaged velocity, $U_{max}(x_i)$ is the maximum value of U along the ith vertical, x_i is the distance of the ith sampled vertical from the left bank, $h(x_i)$ is the dip (i.e., the depth of $U_{max}(x_i)$ below the water surface), $D(x_i)$ the flow depth, y is the vertical distance from the bed. The relationship between the entropic parameter, M, and the entropic function, $\phi(M)$, is (Chiu, 1989):

$$\phi(M) = \frac{U_m}{U_{MAX}} = \frac{e^M}{e^M - 1} - \frac{1}{M} \tag{2}$$

205   in which U_m and U_{MAX} are the average and maximum flow velocities within the entire cross-section. It is worth mentioning that U_m represents the expected value of velocity that can be different from the observed mean velocity (Marini and Fontana, 2020). These two values are quite similar in the case of wide rivers (aspect ratio larger than 5). In the present research, considering the large aspect ratio for all cross-sections (Table 2), this hypothesis is valid.

Introducing the variable $\delta(x_i) = D(x_i)/[D(x_i) - h(x_i)]$, the velocity dip, $h(x_i)$, is estimated according to Yang et al. (2004)

210   from the spanwise distribution of $\delta(x_i)$, which is given as

$$\delta(x_i) = 1 + 1.3 \exp\left(-\frac{x_{min}}{D(x_i)}\right) \tag{3}$$

in which x_{min} is the spanwise distance of the x_i vertical from the nearest bank. Note that $h(x_i) = 0$ and $\delta(x_i) = 1$ when the maximum velocity occurs at the free-surface.

In case of gauged cross-sections, $\phi(M)$ can be inferred from measured mean and maximum flow velocities (e.g., with ADCP). For ungauged sites $\phi(M)$ can be estimated as (Moramarco and Singh, 2010):

$$\phi(M) = \frac{\frac{1}{n} R^{1/6}}{\sqrt{g} \frac{1}{k} \ln\left(\frac{D-h}{y_0}\right)} \tag{4}$$

215   where y_0 is the vertical coordinate, taken from the bottom, where the velocity is zero, k is the von Karman constant, R is the hydraulic radius, n is the Manning roughness, D is the maximum water depth, and h is computed with Eq. (3) at the talweg, i.e., where the water depth is maximum. According to van Rijn (1982), $y_0 = 0.065\ \xi\ d_{90}$, where d_{90} is the 90th percentile for grain size and ξ a parameter ranging from 1 to 10 (Ferro, 2003; Moramarco and Singh, 2010).

Whether at a river site only the surface velocities, $U_{surf}(x_i)$, are available, then $U_{max}(x_i)$ can be estimated as (Fulton and

220   Ostrowski, 2008):

$$U_{max}(x_i) = \frac{U_{surf}(x_i)}{\frac{1}{M} \ln[1 + (e^M - 1)\delta(x_i)e^{1-\delta(x_i)}]} \tag{5}$$

For the current research, the methodological steps to estimate the cross-sectional velocity distribution (and hence the flow discharge) using the entropy theory, are as follows. The input data is the river-wide velocity distribution at the free-surface, U_{surf}, provided by the 3D-CFD model. When only the maximum value of U_{surf} is used as input, corresponding to the hypothetical case in which only point-sensor data are available, the spanwise distribution of U_{surf} is obtained by applying either

225   a parabolic or an elliptical spanwise distribution (Bahmanpouri et al., 2022a). The velocity dip is computed using Eq. (3). The cross-sectional velocity distribution is then obtained using an iterative procedure, in which p ~~denote~~denotes the iteration. At the first iteration, the entropic function, $\phi(M)_{p=1}$, is computed with Eq. (4), and $M_{p=1}$ is computed with Eq. (2). After computing the maximum velocity for each vertical, $U_{max}(x_i)_{p=1}$, with Eq. (5), Eq. (1) allows estimating the entropic velocity distribution in the whole cross-section, $U(x_i, y)_{p=1}$. The following iteration starts by computing the average and the maximum flow

230   velocities, U_m and U_{MAX}, from the velocity distribution obtained in the previous iteration, then $\phi(M)_p = U_m/U_{MAX}$, M_p using Eq.

(2), $U_{max}(x_i)_p$ with Eq. (5), and the velocity distribution $U(x_i, y)_p$ with Eq. (1). The iterative procedure continues until the error of $\phi(M)_p - \phi(M)_{p-1}$ becomes lower than 0.01. For more details, the reader is referred to Moramarco et al. (2017).

3 Results and discussions

The comparison between the entropy-based and the CFD-derived velocity distributions has been performed considering four
235   cross-sections (Figure 2), at a distance of 50 m upstream and 50, 100, and 200 m downstream of the bridge, and the three flood events of 2012, 2019, and 2022 (see Table 1). The sections just upstream and downstream of the bridge are located at a distance of about $0.45B$ from the bridge, with B the width of the river at the bridge section. This is a short distance, particularly considering that the remote sensors for surface velocity (such as radar, Large Scale PIV, etc.) have their field of view located some tens of meter upstream or downstream of the bridge. The sections far downstream are considered to assess how far the
240   flow field is affected by the presence of the bridge.
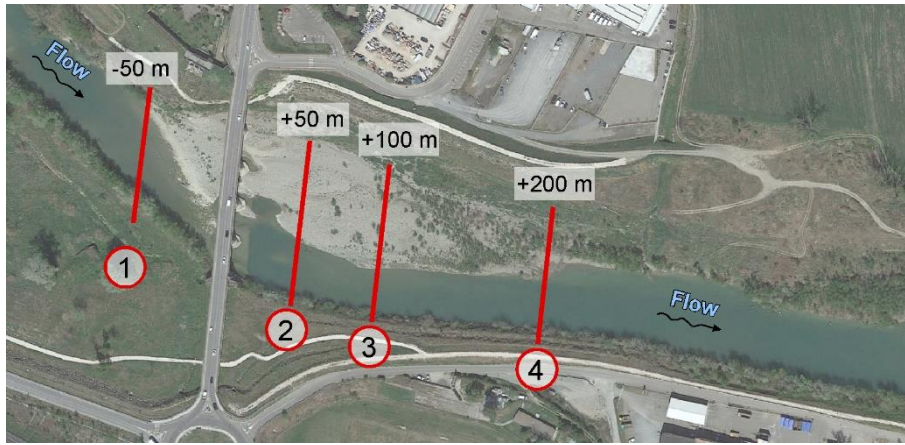
Figure 2. Location of the Adunata Bridge and of the four selected cross-sections (aerial image from © Google Earth).

First, the study analyzes the variability of the entropy function, $\phi(M)$, at the four cross-sections, as derived from the cross-sectional velocity distributions provided by both the 3D-CFD model and the current meter measures (Sect. 3.1). Then, in
245   applying the entropy model to estimate the cross-sectional velocity, two different procedures are considered. In the first one, the entropy model was forced with the river-wide distribution of the surface velocities computed by the 3D-CFD model (this is described in the following Sect. 3.2); in the second one, only the maximum value of the surface velocity computed by the 3D-CFD model was considered as input for the entropy model (Sect. 3.3). The first procedure was applied to all the four cross-sections, whereas the latter was only applied to cross-sections 1 and 4, i.e., where the effects of the bridge piers are minimal
250   so that the spanwise velocity distribution is unimodal.

3.1 Variability of the entropy function

Some relevant parameters that characterize the flow field (e.g., aspect ratio, average and maximum velocity) at the selected cross-sections are presented in Table 2 for the peak flow condition of the three flood events. The values of the entropic function, $\phi(M)_{CFD}$, were first computed as the ratio of average to maximum velocity within the cross-section provided by the 3D-CFD model. Then, assuming the site as ungauged, $\phi(M)_{Eq\,(4)}$ were estimated using Eq. (4) with $d_{90} = 0.01$ m (Pilbala et al., 2024) and a Manning parameter, n, equal to 0.035 m$^{-1/3}$s at the upstream (-50 m) and far downstream sections ($+100$ m and $+200$ m), and equal to 0.055 m$^{-1/3}$s just downstream of the bridge ($+50$ m cross-section) where larger energy losses are expected because of the wakes generated by the bridge piers. The values of $\phi(M)_{Eq\,(4)}$ reported in Table 2, corresponding with the points marked with dashed lines in Figure 3b, were obtained using $\xi = 5$ to compute y_0 (Sect. 2.5 just after Eq. (4)), and the grey band was obtained by varying ξ in the range [1,10]. Finally, the values of the entropic parameter associated to the different values of $\phi(M)$ are computed using Eq. (2).

Year	Distance from the bridge (m)	Channel aspect ratio (width/depth)	Average Velocity (m/s)	Maximum Velocity (m/s)	$\phi(M)_{CFD}$	M_{CFD}	$\phi(M)_{Eq\,(4)}$	$M_{Eq\,(4)}$
	-50	9.26	4.43	6.82	0.650	1.91	0.659	2.04
2012	$+50$	13.78	2.91	7.01	0.415	-1.03	0.410	-1.10
	$+100$	11.05	3.61	6.68	0.541	0.50	0.643	1.81
	$+200$	8.5	4.06	5.48	0.740	3.4	0.642	1.80
	-50	16.3	3.0	4.21	0.711	2.87	0.635	1.70
2019	$+50$	18.45	1.93	3.74	0.515	0.18	0.405	-1.16
	$+100$	14.75	2.08	3.26	0.639	1.75	0.630	1.70
	$+200$	12.84	2.40	3.47	0.690	2.51	0.609	1.35
	-50	27.7	2.57	3.40	0.755	3.71	0.625	1.56
2022	$+50$	27.3	1.33	2.58	0.514	0.17	0.395	-1.29
	$+100$	20.9	1.55	2.19	0.711	2.86	0.612	1.39
	$+200$	13.23	1.97	2.56	0.767	3.96	0.619	1.48

Table 2. Flow data for the cross-sections of Figure 2 and the three considered flood events of Table 1. The values of the entropic function, $\phi(M)$, and parameter, M, are obtained from the 3D-CFD velocity distributions and estimated according to Eq. (4).

Since the entropic function is typically assumed to be constant for all flow conditions at a given cross-section, it is of interest to analyze its actual variation by exploiting the flow fields provided by the 3D-CFD model, and to see the effectiveness of their first-guess estimates obtained using Eq. (4). The values of $\phi(M)$ reported in Table 2 are plotted in Figure 3 as a function of the downstream distance from the bridge. At the first cross-section downstream of the bridge (i.e., cross-section 2), although referring to different flow conditions, values of the entropic function computed with the 3D-CFD and the current meter velocity distributions show the same magnitude, further confirming the reliability of the 3D-CFD model. The first-guess estimates of $\phi(M)$ in Figure 3b, although having a marginal role on the entropy-based computations, show a similar trend to the 3D-CFD

For each flood event, at cross-sections 1 and 4, i.e., where the flow field is not characterized by the wakes generated by the bridge piers, the entropic function assumes similar values, which can be identified as "undisturbed" values. The variability of

275   such undisturbed values of $\phi(M)$ with the flowrate is relatively small, as all the values fall in the range $0.65 < \phi(M) < 0.75$, which is in agreement with the range found by Bahmanpouri et al. (2022b) for similar European rivers. On the contrary, at cross-sections 2 and 3, just downstream of the bridge, the values of $\phi(M)$ are consistently reduced due to the effect of the bridge. At cross-section 2, for the flood conditions of 2012, $\phi(M)_{CFD}$ equals to 0.415, which leads to $M_{CFD} = -1.03$. The low value of $\phi(M)$ and the negative value of M attest the strongly non-uniform distribution of the velocity (i.e., the maximum

280   velocity in this cross-section is much higher than the average velocity). For the moderate peak flows of 2019 and 2022 event, the entropic function recovers undisturbed values already at cross-section 3, i.e., 100 m downstream of the bridge. In the largest flood event of 2012, which produced near pressure-flow conditions at the bridge with marked localized increasing of the flow velocity, $\phi(M)$ decreases from 0.64 to 0.42, and a sensible reduction is still present 100 m downstream of the bridge (cross-section 3).
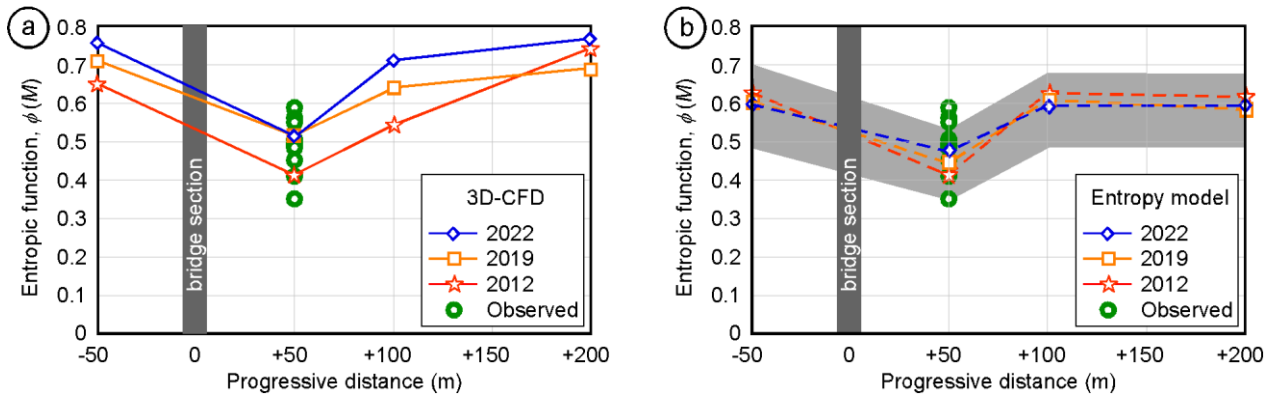
285

Figure 3. Entropic function $\phi(M)$, for the different simulated scenarios, as a function of the distance from the bridge (positive downstream), (a) computed from the 3D-CFD flow fields and (b) estimated with Eq. (4), where the lines refer to the average values and the gray band is obtained by varying the reference height y_0 in Eq. (4) within the expected range. Green circles refer to data derived from velocity distributions measured with the current meter just downstream of the bridge.

290   This first analysis suggests that assuming constant values of $\phi(M)$ can be reasonable in undisturbed river reaches; however, in case of irregular flow fields induced by the interactions with in-stream structures, the entropic function $\phi(M)$ can vary with respect to undisturbed values and, in addition, it can show significant variations with the flowrate.

3.2 Entropy model forced with the river-wide profile of free-surface velocity

The efficacy of the entropy model is here tested for the case in which the surface velocity is known for all the width of the

295   cross-section. This could be the case in which the river-wide surface velocity is estimated from imaging techniques (e.g., Eltner

et al., 2020; Schweitzer and Cowen, 2021). The results, in terms of cross-sectional velocity distributions, are presented for brevity only for the intermediate peak flow of the 2019 flood event, and for the most challenging cross-sections just downstream of the bridge, where the flow field is disturbed by the pier wakes. The same results, for the peak flows of 2012 and 2022 events, are provided as supplementary material.

300   Figure 4 presents the cross-sectional velocity distribution 50 m downstream of the bridge (cross-section 2). As shown by the 3D-CFD flow field (Fig. 4a) and reflected in the low value of $\phi(M)$ for this cross-section (Table 2 and Figure 3), the effect of the piers is very strong, such that there is a clearly uneven distribution of the cross-sectional velocity because of the wakes developing downstream the piers. Despite that, using as input the river-wide distribution of the surface velocity provided by the CFD simulation, the entropy model can reliably capture the salient features of the cross-sectional velocity distribution.
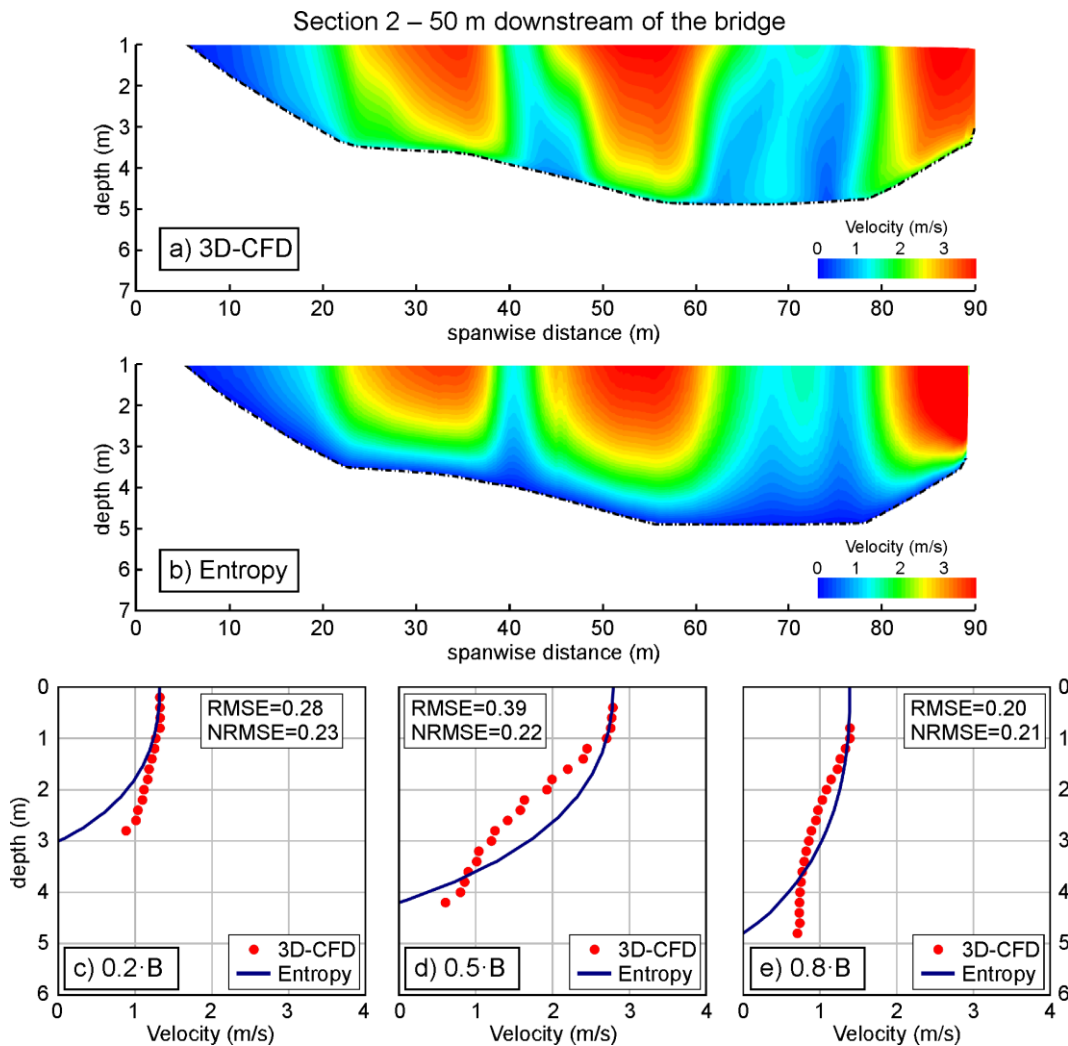
305

Figure 4. Flood event of 2019, cross-section 2 (50 m downstream of the bridge). Velocity distributions provided by (a) the 3D-CFD model, and (b) the entropy model forced with the river-wide distribution of the free-surface velocity. Comparison of vertical distributions of velocity at 0.2B (c), 0.5B (d), and 0.8B (e), where B is the width of the cross-section.

Figure 4(c-e) highlights the comparison of 3D-CFD and entropy flow velocities along three verticals located at 0.2 B, 0.5 B,

310 and 0.8 B (where B is the channel width). Compared to the results of the 3D-CFD model, the entropy approach underestimates the velocity close to the bed. Just downstream of the bridge, due to the presence of the bridge arches, the flow field provided by the 3D-CFD model is configured as a sort of partial orifice flow that increases the vertical uniformity of the velocity distribution compared to a uniform shear flow. Of course, the entropy model cannot capture such a localized flow features, which entails some difference in the patchiness of the physics-based and the entropy velocity distributions (Figure 4a-e). Since

315 the velocities and the volumetric fluxes are still relatively small near the bed, these discrepancies marginally affect the estimation of the section-averaged velocity and, consequently, of the total discharge (Table 3). The percentage error is quite

larger (7.6%) for the very high-flow condition of the 2012 event (see Supplementary Materials), due to the accentuation of orifice-flow conditions associated to the higher water levels.

Figure 5 depicts the cross-sectional velocity distributions at a larger distance from the bridge, i.e. at cross-section 3, placed
320   100 m downstream the bridge. The visual comparison with Figure 4 suggests that the effects of the piers on the flow field are reduced because of the increased distance, and the cross-sectional distribution provided by the 3D-CFD model (Figure 5a) appears more regular. The statistical analysis confirms that in this case the entropy model (Figure 5b) is able to simulate the velocity profiles with a higher accuracy.
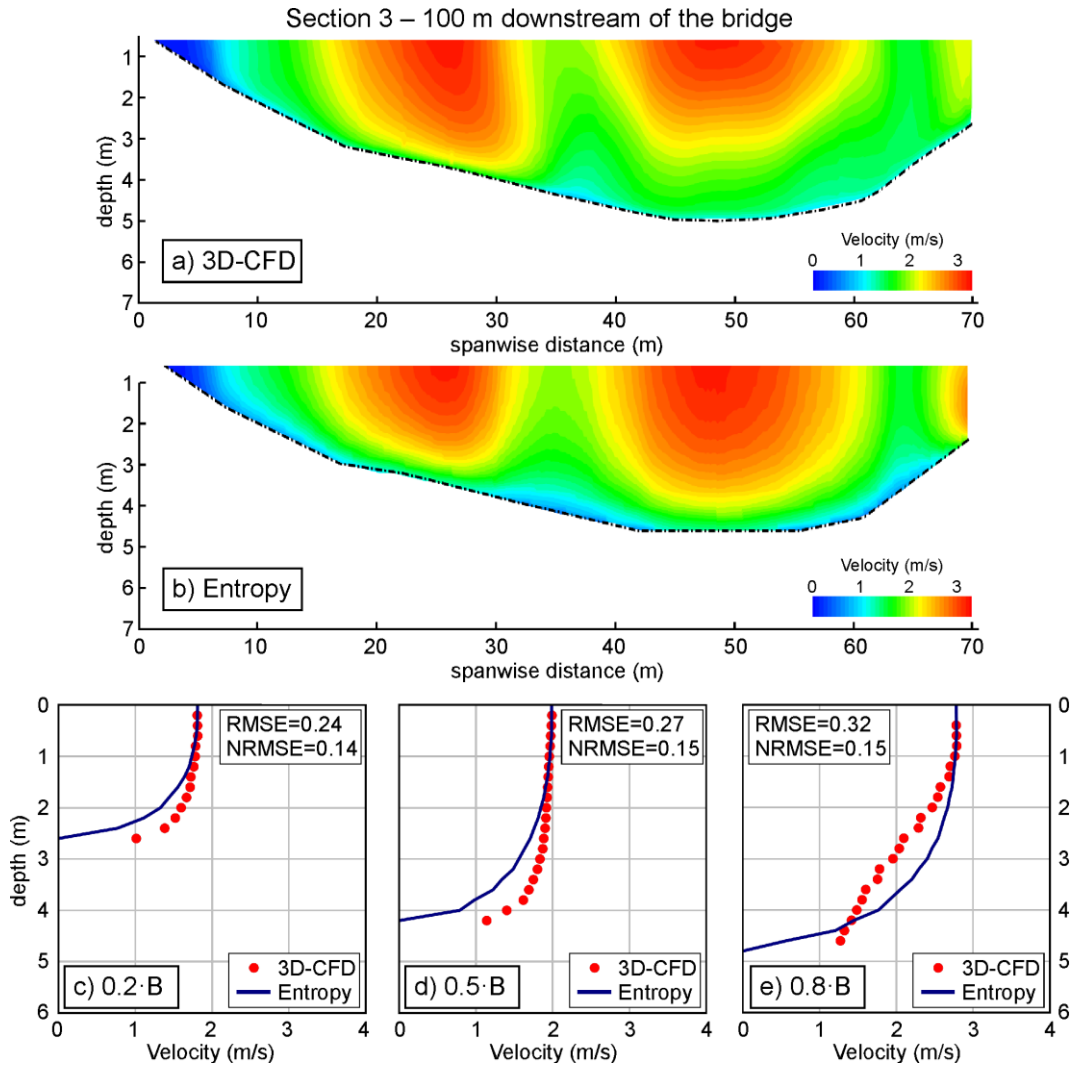
325   **Figure 5. Flood event of 2019, cross-section 3 (100 m downstream of the bridge). Velocity distributions provided by (a) the 3D-CFD model, and (b) the entropy model forced with the river-wide distribution of the free-surface velocity. Comparison of vertical distributions of velocity at 0.2B (c), 0.5B (d), and 0.8B (e), where B is the width of the cross-section.**

Figure 6 shows the cross-sectional velocity distributions of 3D-CFD and entropy models for the cross-section 4, i.e. 200 m downstream of the bridge. Compared to cross-section 3, the effect of the bridge piers is further reduced, because of both the

330 distance and the more compact shape of the cross-section. Since the effect of the bridge piers is minimum, the statistical analysis shows a better agreement of the entropy model results with the CFD-based data. Though areas with high velocities are still visible in simulations with higher values of the discharge (i.e., events of 2012 and 2019), for the high-flow conditions of 2022, the effect of the bridge pier has completely vanished. Therefore, the lower the flow discharge the lower the distance from the bridge to reach the normal flow condition without the bridge effect.
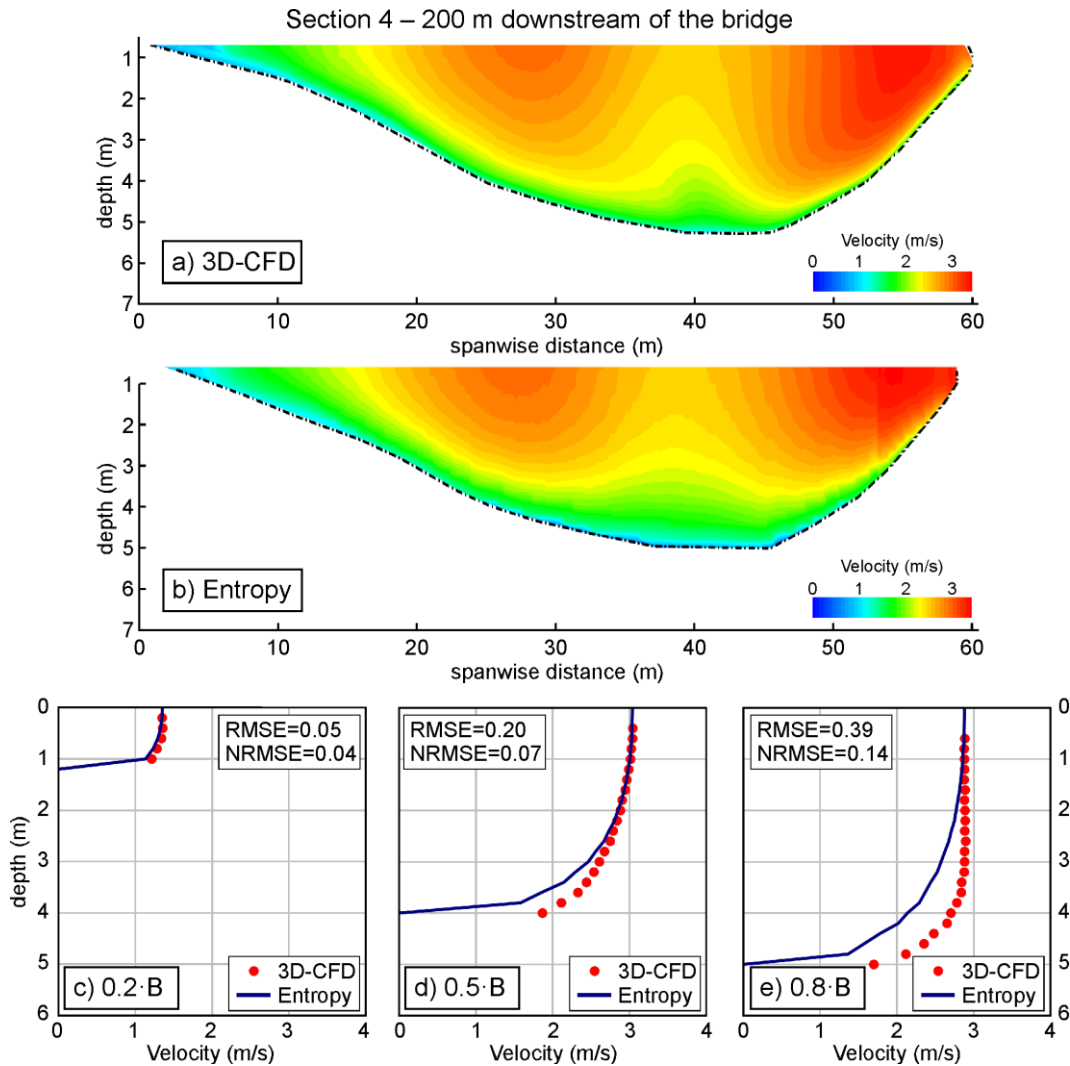
335

Figure 6. Flood event of 2019, cross-section 4 (200 m downstream of the bridge). Velocity distributions provided by (a) the 3D-CFD model, and (b) the entropy model forced with the river-wide distribution of the free-surface velocity. Comparison of vertical distributions of velocity at 0.2*B* (c), 0.5*B* (d), and 0.8*B* (e), where *B* is the width of the cross-section.

The results here presented show that, when the river-wide distribution of the free-surface velocity is provided, the entropy
340 method allows to provide good estimations of the cross-sectional velocity distribution even when the influence of bridge piers, and thus the unevenness of the flow field, is relevant. The main discrepancies are observed in the regions of flow with low values of velocity, which slightly affect the estimation of the flow discharge. Table 3 lists some statistics and error percentages for the depth-averaged velocity and discharge estimates for all cross-section and the three events considered. The estimation provided by the entropy method are in good agreement with results of CFD model, both upstream and downstream of the
345 Adunata bridge. Though the accuracy is slightly reduced downstream of the bridge, the results are reliable also in the vicinity of the structure (i.e., at cross-section 2), suggesting the applicability of the entropy model to estimate the flow discharges even in case of irregular distributions of the cross-sectional velocity, provided that the river-wide distribution of the surface velocity is used as input data.

Flood event	Cross-section	Distance from the bridge (m)	Average velocity (m/s)		Discharge (m³/s)		Error percentage (%)
			3D-CFD	Entropy	3D-CFD	Entropy	
2012	1	−50	4.43	4.64	1'800	1'885	+4.7
	2	+50	2.91	2.69		1'664	−7.6
	3	+100	3.61	3.54		1'765	−2.0
	4	+200	4.06	4.30		1'906	+5.9
2019	1	−50	3.0	3.0	450	450	+0.1
	2	+50	1.93	1.90		443	−1.5
	3	+100	2.08	2.12		459	+2.0
	4	+200	2.40	2.54		476	+5.8
2022	1	−50	2.57	2.66	160	166	+3.7
	2	+50	1.33	1.24		150	−6.3
	3	+100	1.55	1.51		157	−1.9
	4	+200	1.97	1.98		161	+0.6

350 **Table 3. ~~Flood event of 2019.~~ Comparison between 3D-CFD outputs and entropy-based estimations forced with the river-wide distribution of the free-surface velocity.**

3.3 Entropy model forced with a single value of free-surface velocity

In this section, the results are presented considering only a single value of the surface velocity as input for the entropy model, which corresponds to the maximum surface velocity predicted by the 3D-CFD model. Two different spanwise velocity
355 distributions are enforced in the entropic model, namely a parabolic spanwise distribution (PSD) and an elliptic spanwise distribution (ESD). Of course, applying the entropy model using a unique value of the velocity is particularly sensitive of this value and ~~suppose~~supposes a unimodal velocity distribution in the spanwise direction. For this reason, this kind of approach cannot be used in the cross-sections immediately downstream the bridge, where velocities show large spatial variations (see e.g., Figure 4). Herein, the results are presented for cross-section 1, i.e. 50 m upstream of the bridge for the high-flow condition

360 of the 2012 event, and for cross-section 4, i.e. 200 m downstream of the bridge for the modest peak flow condition of the 2022 event, where the effect of bridge piers on the velocity distribution wears off in a shorter distance.

Figure 7 shows the distribution of the surface velocity based on CFD outputs and both the PSD and ESD entropy models. The agreement of both the PSD and the ESD is generally good in the central and the right parts of the channel, and less good in the left part of the channel. Here, due to the irregular bathymetry (i.e., gravel deposit), the 3D-CFD model predicts localized

365 stagnation zones that cannot be captured by the entropy model based on a single value of the surface velocity. This is confirmed by Figure 8a,, which shows the cross-sectional distribution of the ~~depth average~~surface velocity and three vertical profiles. In the perspective of estimating the flow discharge, the lateral discrepancies represent a minor limit, as the central part of the cross-sections conveys the largest part of the total discharge.
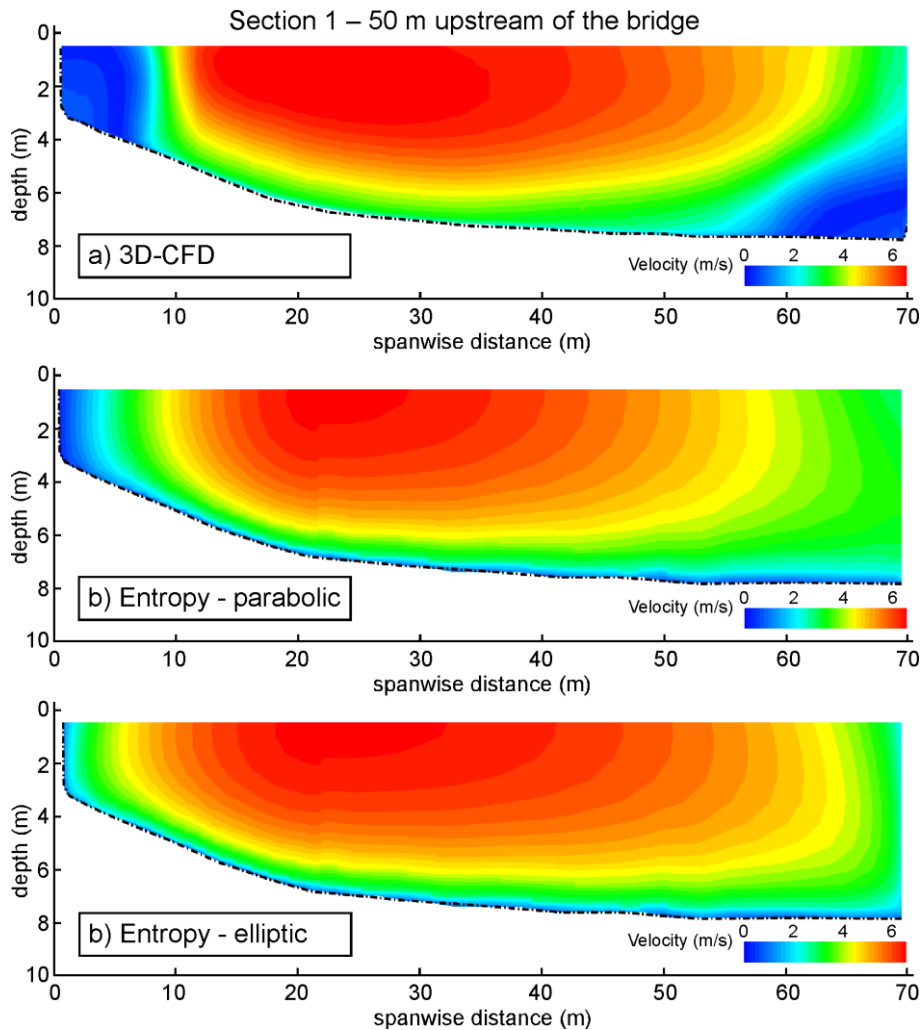
370 **Figure 7. Flood event of 2012, cross-section 1 (50 m upstream of the bridge). Cross-sectional velocity distribution computed with the 3D-CFD model (a), the entropy theory with parabolic (b) and elliptic (c) spanwise velocity distribution.**

Overall, the cross-sectional velocity distributions based on ESD seem more accurate than those based on the PSD: they provide similar results at the center of the channel, but the parabolic distribution generally underestimates the flow velocity close to the banks. Both cross-sectional and vertical distributions of the velocity profiles (Figure 7a and Figure 8c) highlight the

375 existence of a velocity dip, i.e. the maximum velocity is below the water surface, particularly at the center of the channel. This is generally the consequence of secondary currents superposed to the main flow (Termini and Moramarco, 2020). Yang et al. (2004) and Moramarco et al. (2017) reported that for large aspect ratios of channel flow, B/D, the dip phenomenon appears primarily near the sidewall region, whereas for relatively low aspect ratios (B/D = 9.26 for cross-section 1) the velocity dip is generally located at the center of the channel (Bahmanpouri et al., 2022a,b; Kundu and Ghoshal, 2018; Moramarco et al., 2017;

380 Termini and Moramarco, 2020). In this case, the 3D flow field from the CFD simulation shows that the dip depends on the counter-clockwise rotating secondary current generated by the upstream right-handed bend. Indeed, rotational inertia makes these curvature-induced helical flow structures to propagate downstream for relatively long distances (Dominguez Ruben et al., 2021; Lazzarin and Viero, 2023; Thorne et al., 1985).
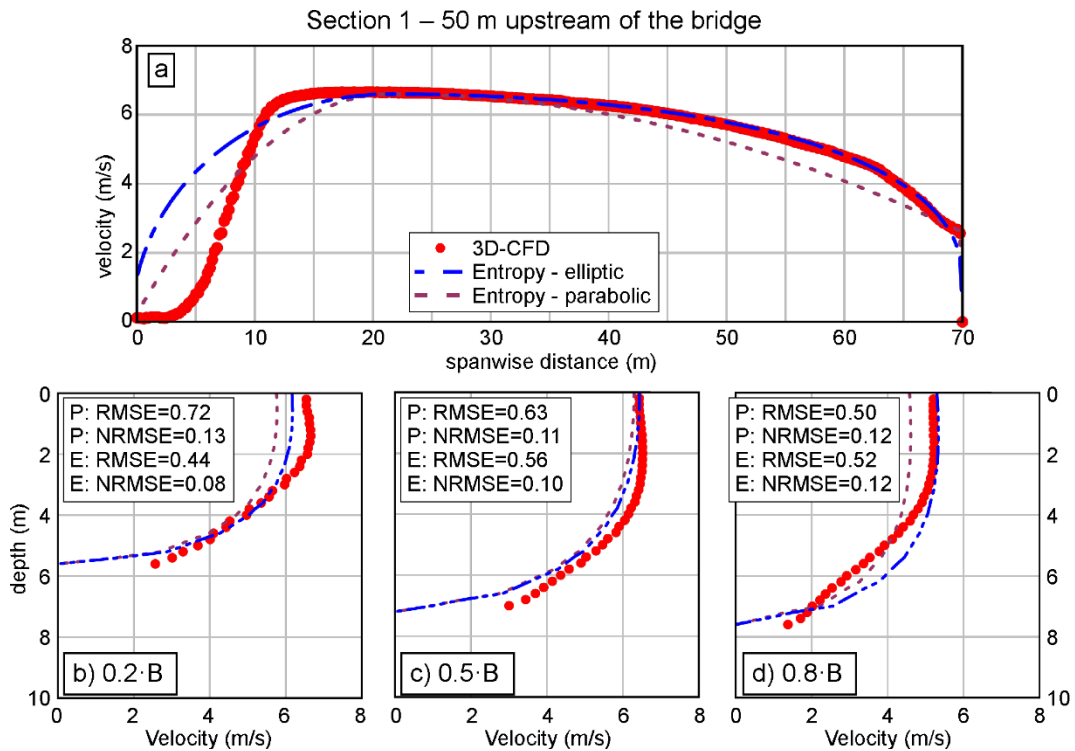
385 **Figure 8. Flood event of 2012, cross-section 1 (50 m upstream of the bridge). Spanwise distribution of the surface velocity (a); comparison of vertical distributions of velocity at 0.2B (b), 0.5B (c), and 0.8B (d).**

The distribution of the velocity ~~at the free surface~~ for the cross-section 4 (200 m downstream of the bridge) is presented in Figure 9 for the moderate peak flow condition of the 2022 event. For this cross-section, in the 3D-CFD results (Figure 9a), the maximum surface velocity is located on the left side of the channel, rather than at its center (this aspect is discussed in the

390   following). Forced with the maximum water surface velocity, the entropy model well reproduces the velocity field in the central part of the riverbed. Larger discrepancies are instead observed in the lateral part of the cross-section, with the elliptic spanwise distribution (ESD) that performs slightly better than the parabolic (PSD), particularly in the right side. Figure 10 shows the cross-sectional distribution of the ~~depth-averaged~~surface velocity and the velocity distribution along three verticals. In terms of cross-sectional average velocity and flow discharge, both the PSD and ESD produce error that are lower than 10%

395   (Table 4), then quite larger than those obtained using the river-wide surface velocity as input for the entropy model.
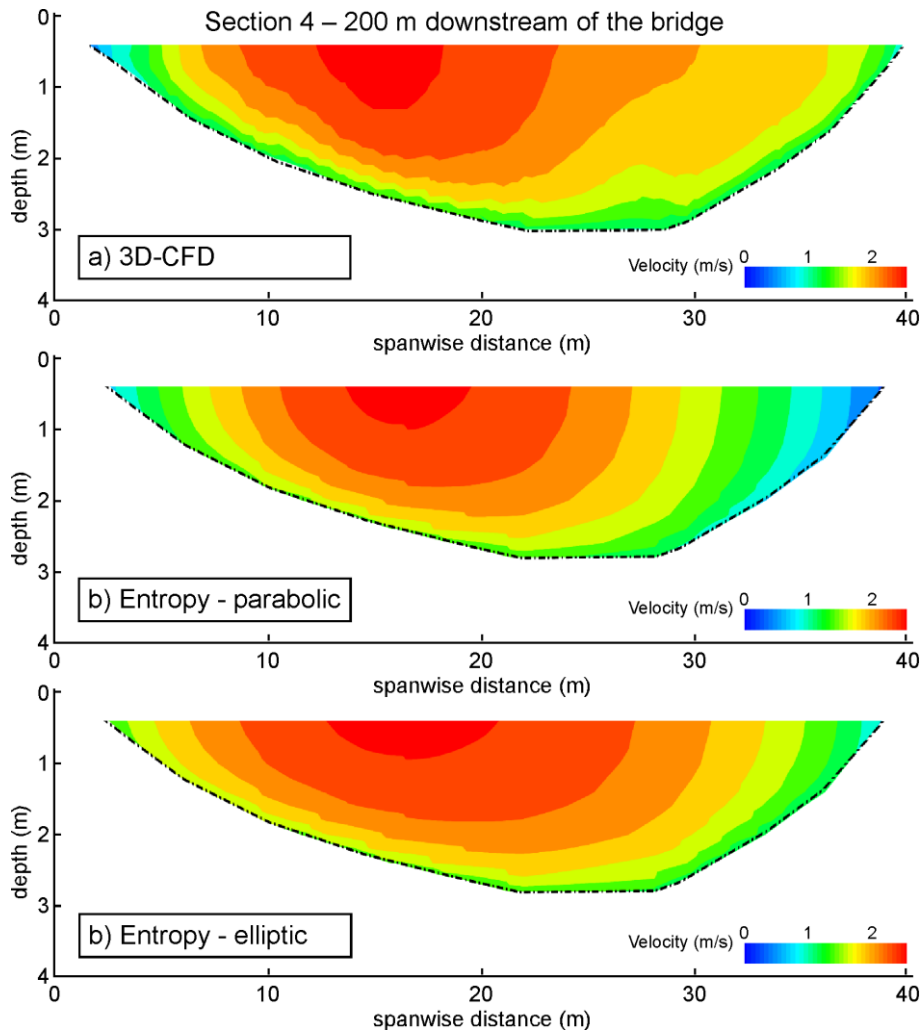
Figure 9. Flood event of 2022, cross-section 4 (200 m downstream of the bridge). Cross-sectional velocity distribution computed with the 3D-CFD model (a), the entropy theory with parabolic (b) and elliptic (c) spanwise velocity distribution.

A last point worth of discussing regards the unusual cross-sectional distribution of flow velocity at section 4 (Figure 9a). The

400   reason why the 3D-CFD model locates the maximum velocity at the left of the talweg is the alternate vortex shedding occurring downstream of the bridge piers, which propagates beyond the last considered cross-section. This is evident in the map of

instantaneous surface-velocity of Figure 11. This particular occurrence poses interesting questions on the application of the entropy model to estimate the flow discharge downstream of in-stream structures. First, the spanwise location of the maximum surface velocity is subject to a periodical shift, which prevents its correct detection by means of a fixed sensor with a small-size field of view, like the one mounted on the Adunata bridge. Secondly, marked time-varying flow fields, which occasionally (or periodically) deviate from nearly uniform flow conditions, can hardly be captured by any preset velocity distribution. To alleviate the problem, the periodic signal of surface velocity can be filtered, which is equivalent to look at time-averaged modelled flow fields, which requires knowing the frequency of vortex shedding.
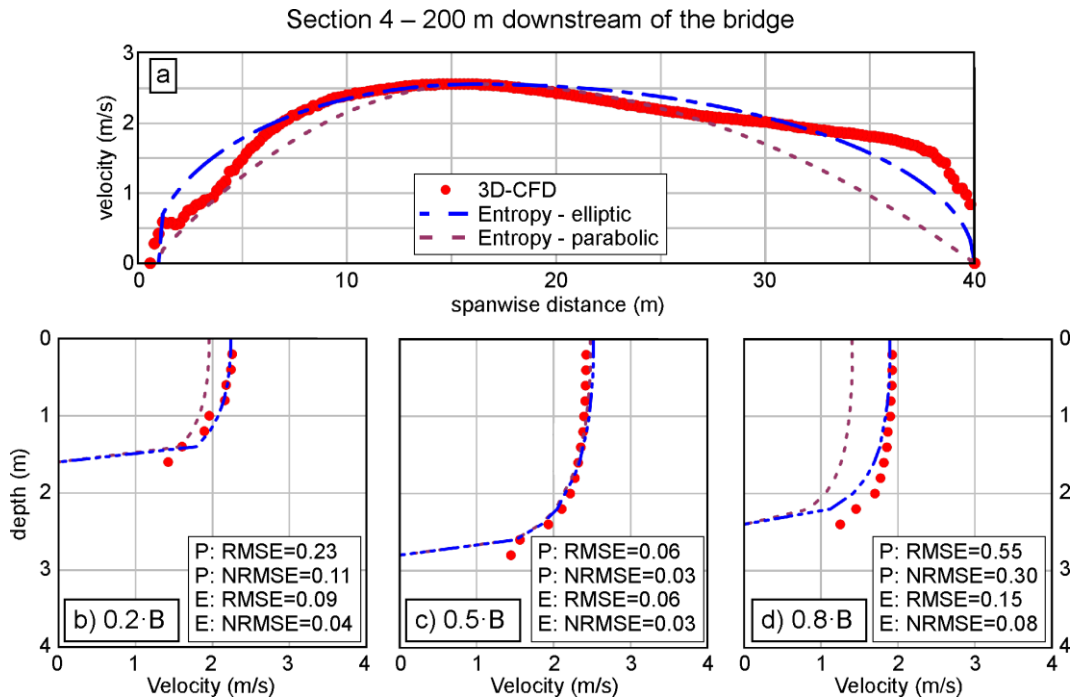
Figure 10. Flood event of 2022, cross-section 4 (200 m downstream of the bridge). Spanwise distribution of the surface velocity (a); comparison of vertical distributions of velocity at 0.2B (b), 0.5B (c), and 0.8B (d).
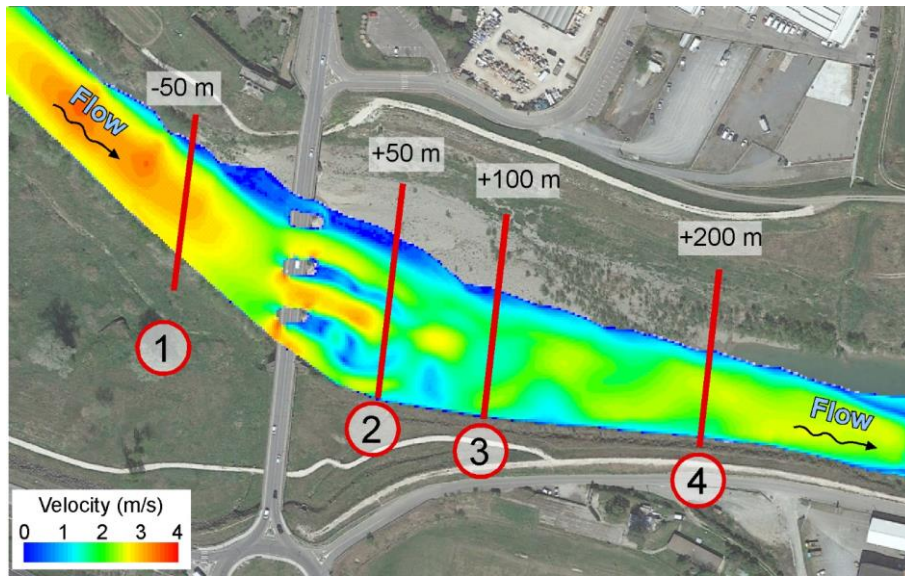
Figure 11. Flood event of 2022. Colormap of the instantaneous surface velocities computed with the 3D-CFD model for the Paglia River at the Adunata bridge (aerial image from © Google Earth).

The results shown in this Section confirm the general accuracy of the entropy model in predicting the velocity distributions. As expected, when using a single value of velocity in place of the river-wide distribution of surface velocity, the accuracy of the method decreases. Provided that using a single velocity is beyond the scope of the method when the velocity distribution is markedly irregular, the entropy approach can still be forced with a single surface velocity, and produce accurate results, when there are no evidences of strong disturbances of the flow. Indeed, such an approach cannot capture marked unevenness in the flow field, as shown in the case of the lateral low-velocity regions at cross-section 1 for the 2012 event (Figure 7), and in the time-varying flow field of cross-section 4 for the 2022 event (Figure 9).

Distance from the bridge (m) and year	Average velocity (m/s)			Discharge (m³/s)			Error percentage (%)	
	3D-CFD	Entropy		3D-CFD	Entropy		Parabolic	Elliptic
		Parabolic	Elliptic		Parabolic	Elliptic		
−50 (2012)	4.43	4.44	4.83	1'800	1'804	1'962	+0.2	+9.0
−50 (2019)	3.00	3.24	3.40	450	486	510	+8.0	+13.3
−50 (2022)	2.55	2.65	2.74	160	166	172	+3.8	+7.5
+200 (2022)	1.97	1.81	2.02	160	147	164	−8.0	+2.0

Table 4. Comparison between 3D-CFD and entropy-based outputs considering a single surface velocity.

4 Conclusions

The present study investigated the ability of the entropy-based method to estimate the cross-sectional distribution of velocity, as well as the associated river discharge, for different flow conditions in a representative case study. As sensors for continuous

monitoring of water level and surface velocity are often mounted on existing bridges, a stretch of the Paglia River was analyzed where a multi-arch bridge with thick piers, which hosts a level gauge and a radar sensor, strongly affects the flow field.

With the goal of assessing the applicability of the entropy model in case of flows disturbed by the presence of in-stream
430   structures, a 3D-CFD model was set up to obtain reliable, physics-based velocity distributions at relevant cross-sections, both upstream and downstream of the bridge. The entropy model was then applied to reproduce this set of velocity distributions, using the bathymetric data and the CFD-computed surface velocity as input.

As a first point, the study highlighted the potential of using accurate, physics-based, 3D-CFD models to deepen the knowledge of rivers and, specifically, of theoretical methods for discharge estimation. Indeed, 3D-CFD models allows providing pictures
435   of complex flow fields that are more complete than, e.g., ADCP measures, in terms of spatial and temporal distribution and, above all, valid for high-flow regimes which typically prevent any direct measurement of the flow field beneath the free-surface. This entails unexplored chances of outlining best-practices in the use of simplified methods for continuous discharge monitoring, and, as a consequence, to improve their accuracy.

According to the present analysis, the entropy model revealed remarkable skills in reproducing also disturbed and uneven flow
440   fields when the river-wide distribution of the surface velocity is used as input data. This occurred also just downstream of the bridge, where the pier-induced wakes made the velocity distribution multimodal and extremely irregular, with error on discharge estimates lower than 8%. The availability of innovative measuring techniques, able to collect river-wide surface velocity data at a relatively low cost, adds value to the present findings.

On the other side, the accuracy of the entropy model is reduced when only the maximum surface velocity is used as input data,
445   so that the spanwise velocity distribution has to be assumed on a theoretical basis (e.g., parabolic or elliptical). While such a method is absolutely discouraged in case of disturbed flow fields (e.g., downstream of in-stream structures), it still provides accurate estimates where the velocity field is sufficiently regular.

As a final recommendation, measuring instruments and sensors for surface velocity become more effective when placed upstream of in-stream structures, i.e., where the flow field is only marginally affected by the structure and both the water
450   surface elevation and the velocity distribution are far more regular.

A main limitation of the present methodological approach relies in the assumption of fixed bed in both the CFD analysis and the application of the entropic model. In natural rivers, bed scouring during ~~sever~~severe flood events and the ensuing formation of local deposits, especially close to in-stream structures such as bridges, can alter the bathymetry and, in turn, the velocity distribution and the discharge estimates. In case of movable bed and absence of protection measures (e.g., riprap or bed sills),
455   the uncertainty associated to the local bed mobility has to be evaluated with due care.

Future research on more complex scenarios that still need a comprehensive assessment, and which could largely benefit from physics-based numerical modelling, will include the case of mobile beds and the analysis of stage-dependent variations of cross-sectional velocity distribution, particularly in case of compound cross-sections that are typical of natural rivers.

Appendix A

460 To impose the boundary conditions to the 3D-CFD model, a 2D depth-averaged model of a longer stretch of the Paglia River has been setup. We used the 2DEF Finite Element model (Defina, 2003; Lazzarin et al., 2023a, 2024; Viero, 2019; Viero et al., 2013, 2014), which solves a modified version of the shallow water equations (SWEs) that allow for a robust treatment of wetting and drying over irregular topographies (D'Alpaos and Defina, 2007; Defina, 2000). The SWEs are written as:

$$\eta(h_s)\frac{\partial h_s}{\partial t} + \nabla \cdot \mathbf{q} = 0$$

$$g\nabla h_s + \frac{\mathrm{D}}{\mathrm{D}t}\left(\frac{\mathbf{q}}{Y}\right) + \frac{\boldsymbol{\tau}}{\rho Y} - \nabla \cdot \mathbf{Re} = 0$$

(A1)

in which h_s is the free surface elevation, t is the time, ∇ and $\nabla \cdot$ denote the 2D gradient and divergence operators, respectively,

465 $\mathbf{q} = (q_x; q_y)$ is the depth-integrated velocity (i.e., the unit-width discharge), Y is the equivalent water depth (i.e., the volume of water per unit area), and $\eta(h_s)$ a storativity coefficient to account for the wetted fraction of the domain, $\boldsymbol{\tau} = (\tau_x; \tau_y)$ is the bed shear stress, evaluated using the Gauckler-Strickler formula, ρ is the water density, and $\mathbf{Re}$ the horizontal components of the Reynolds stresses, modelled according to the Boussinesq approximation. A mixed Eulerian-Lagrangian approach allows evaluating the total derivative of the flow velocity in the momentum equations using finite differences and a backward tracing

470 technique based on the method of characteristics (Defina, 2003; Giraldo, 2003; Walters and Casulli, 1998). Then, the SWEs are solved with a finite element method, based on triangular, unstructured grids. The model also allows to couple 2D triangular elements with 1D elements (either open- or closed-sections) to model the minor hydraulic network efficiently; other 1D elements are used to model particular devices, such as pumps, weirs, etc. (Martini et al., 2004). The model has been successfully used to simulate flows in various rivers (e.g., Mel et al., 2020a,b; Viero et al., 2019; Baldasso et al., 2023); its effectiveness

475 have been demonstrated also in different research field, such as lagoon and marine environments (e.g., Carniello et al., 2012; Pivato et al., 2020; Tognin et al., 2022; Viero and Defina, 2016).

In the present case, the computational mesh covered a stretch of the Paglia River about 7 km long, from 600 m upstream of the Adunata Bridge to the confluence with the Tiber River, including floodable floodplains (Fig. A1). The average mesh size ranged from 10 m in the riverbed near the Adunata bridge, to 30 m in the floodplains and far downstream of the Adunata

480 bridge. The computational mesh included 61'000 triangular elements, 16 1D elements to simulate underpasses, and 4 1D weir elements to simulate the sill located 500 m downstream of the Adunata Bridge.

The inflow hydrographs, prescribed at the upstream mesh inlet, were derived from water levels measured at the Adunata Bridge using the associated rating curve. At the outlet, an arbitrary rating curve was applied as downstream boundary condition; a sensitivity analysis showed that, because of the distance from the Adunata Bridge, this boundary condition did not produce

485 any perceivable effect in the water levels simulated at the study site.
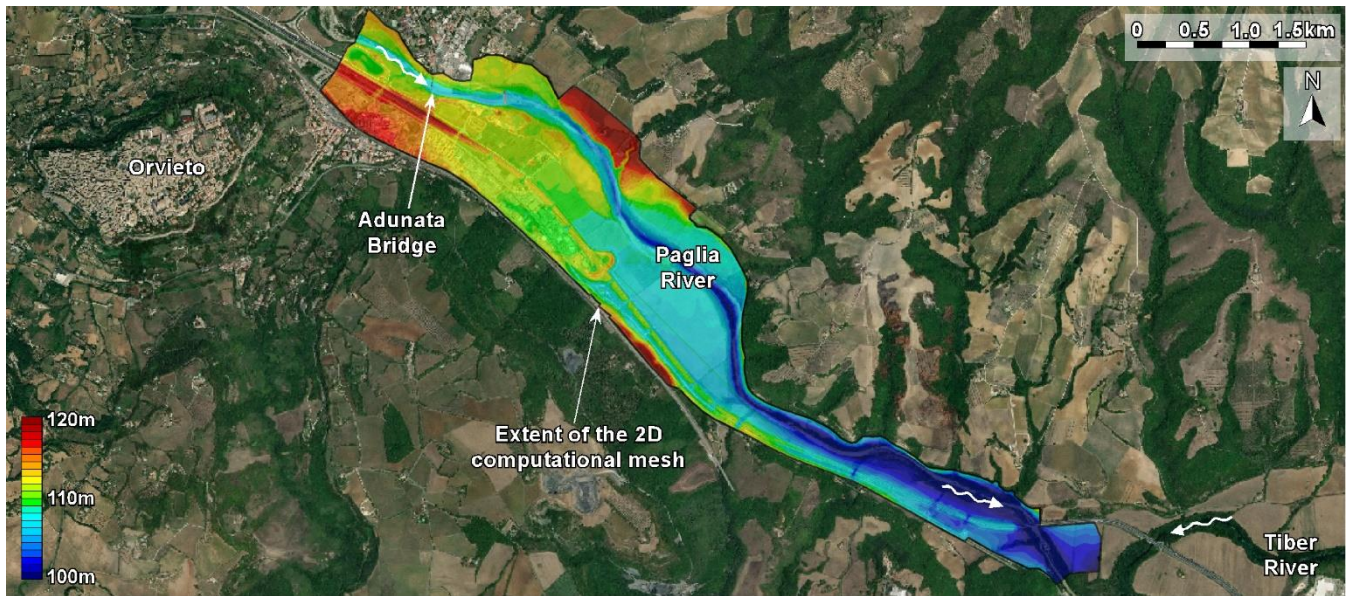
Figure A1. Spatial extent of the 2D computational mesh (aerial image from World Imagery). The color map shows the bottom elevation of the grid elements derived from the LiDAR-based DTM.

Different Gauckler-Strickler coefficients were assigned to the different parts of the domain (e.g., floodplains, densely vegetated areas, etc.) based on the soil cover. The value assigned to the main riverbed were calibrated to match the time series of the water levels measured at the Adunata bridge gauging station for the 2019 flood event (Fig. A2a) and, for the most sever flood event occurred in 2012, the model results were also checked in terms of extent of flooded areas. The minor flood of 2022 was used to verify the model (Fig. A2b). Finally, the depth-averaged velocity just downstream of the Adunata Bridge was compared with the free-surface velocity measured by the radar sensor. Due to the use of a coarse grid and to the depth-average assumption, the 2D model underpredicted the measured water surface systematically (Fig. A2c,d); however, using an amplification factor of 1.7 (gray dots in Fig. A2c,d), the predicted values were quite similar to the measured ones.
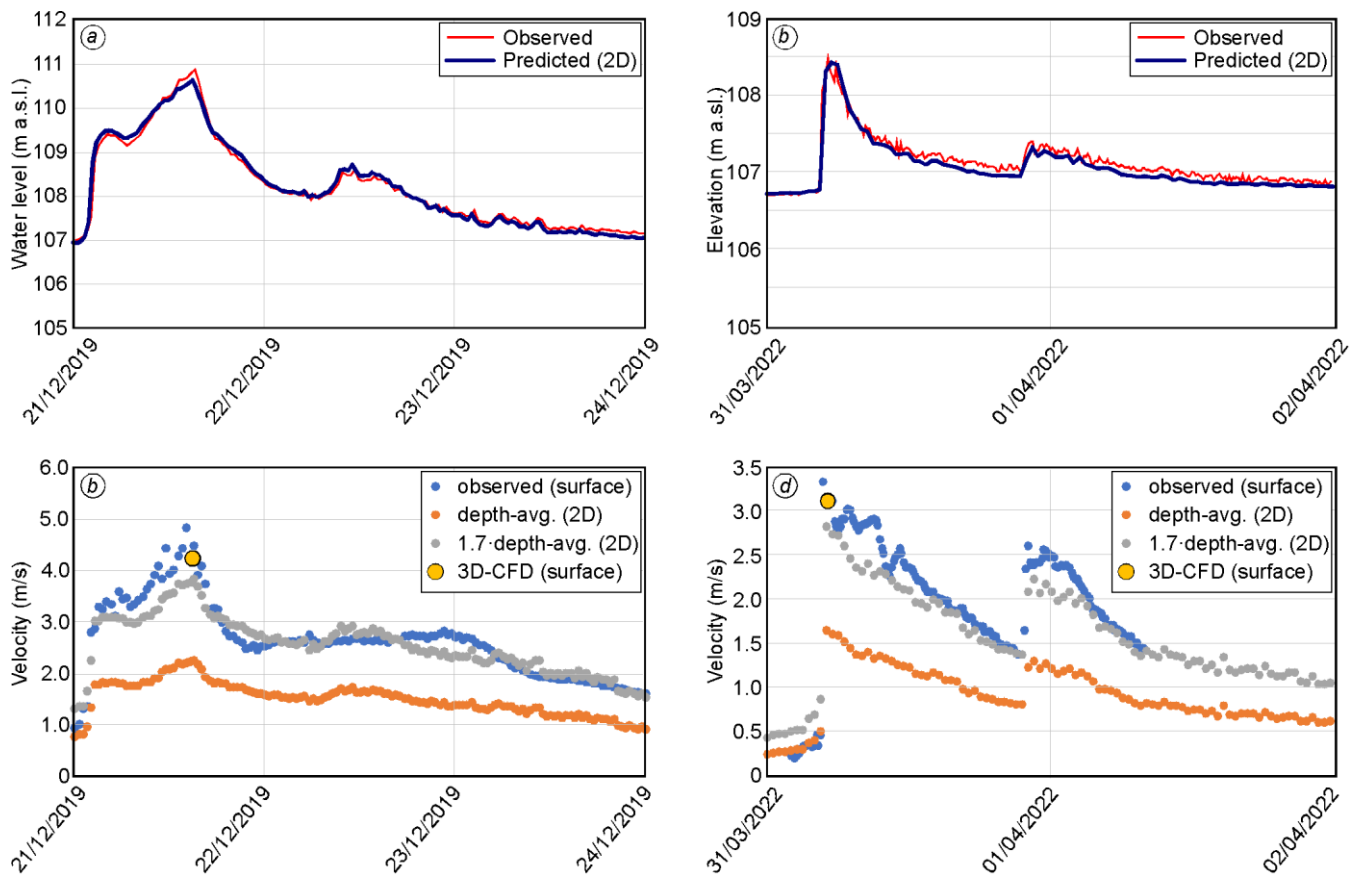
Figure A2. Observed (red) and predicted (blue) water levels at the Adunata Bridge gauging station for the flood events of 2019 (a) and 2022 (b). Observed and predicted water velocity for the flood events of 2019 (c) and 2022 (d).

Data availability

Data available on request from the authors.

Author contribution

Conceptualization: FB, TL, SB, TM, DPV. Formal analysis: FB and TL. Funding acquisition: TM. Investigation: FB and TL. Methodology: FB, TL, SB, TM, DPV. Project administration: SB, TM, DPV. Software: FB, TL, TM, DPV. Supervision: SB, TM, DPV. Visualization FB, TL, DPV. Writing – original draft preparation: FB. Writing – review & editing: TL, SB, TM, DPV.

Competing interests

The authors declare that they have no conflict of interest.

Acknowledgements

510 This study was supported by Italian National Research Programme PRIN 2017, with the project n. 2017SEB7Z8 "IntEractions between hydrodyNamics and bioTic communities in fluvial Ecosystems: advancement in the knowledge and undeRstanding of PRocesses and ecosystem sustainability by the development of novel technologieS with fIeld monitoriNg and laboratory testing (ENTERPRISING)". T.L. is sponsored by a scholarship provided by the CARIPARO foundation. The authors acknowledge the assistance of Luigi di Micco, Shiva Rezazadeh, and Marco Dionigi.

515 **References**

Abdolvandi, A. F., Ziaei, A. N., Moramarco, T., and Singh, V. P.: New approach to computing mean velocity and discharge, Hydrological Sciences Journal, 66, 347–353, https://doi.org/10.1080/02626667.2020.1859115, 2021.

Ammari, A., Bahmanpouri, F., Khelfi, M. E. A., and Moramarco, T.: The regionalizing of the entropy parameter over the north Algerian watersheds: a discharge measurement approach for ungauged river sites, Hydrological Sciences Journal, 67, 1640–520 1655, https://doi.org/10.1080/02626667.2022.2099744, 2022.

Ataie-Ashtiani, B. and Aslani-Kordkandi, A.: Flow field around side-by-side piers with and without a scour hole, European Journal of Mechanics - B/Fluids, 36, 152–166, https://doi.org/10.1016/j.euromechflu.2012.03.007, 2012.

Bahmanpouri, F., Eltner, A., Barbetta, S., Bertalan, L., and Moramarco, T.: Estimating the Average River Cross-Section Velocity by Observing Only One Surface Velocity Value and Calibrating the Entropic Parameter, Water Resources Research, 525 58, e2021WR031821, https://doi.org/10.1029/2021WR031821, 2022a.

Bahmanpouri, F., Barbetta, S., Gualtieri, C., Ianniruberto, M., Filizola, N., Termini, D., and Moramarco, T.: Prediction of river discharges at confluences based on Entropy theory and surface-velocity measurements, Journal of Hydrology, 606, 127404, https://doi.org/10.1016/j.jhydrol.2021.127404, 2022b.

Baldasso, F., Tognin, D., Lazzarin, T., and Viero, D. P.: The role of morphodynamic processes on the Po river conveyance 530 downstream of Pontelagoscuro: a numerical analysis, L'Acqua, 4/2023, 2023.

Bandini, F., Sunding, T. P., Linde, J., Smith, O., Jensen, I. K., Köppl, C. J., Butts, M., and Bauer-Gottwein, P.: Unmanned Aerial System (UAS) observations of water surface elevation in a small stream: Comparison of radar altimetry, LIDAR and photogrammetry techniques, Remote Sensing of Environment, 237, 111487, https://doi.org/10.1016/j.rse.2019.111487, 2020.

Bandini, F., Lüthi, B., Peña-Haro, S., Borst, C., Liu, J., Karagkiolidou, S., Hu, X., Lemaire, G. G., Bjerg, P. L., and Bauer-535 Gottwein, P.: A Drone-Borne Method to Jointly Estimate Discharge and Manning's Roughness of Natural Streams, Water Resources Research, 57, e2020WR028266, https://doi.org/10.1029/2020WR028266, 2021.

Barbetta, S., Camici, S., and Moramarco, T.: A reappraisal of bridge piers scour vulnerability: a case study in the Upper Tiber River basin (central Italy), Journal of Flood Risk Management, 10, 283–300, https://doi.org/10.1111/jfr3.12130, 2017.

Bogning, S., Frappart, F., Blarel, F., Niño, F., Mahé, G., Bricquet, J.-P., Seyler, F., Onguéné, R., Etamé, J., Paiz, M.-C., and
540 Braun, J.-J.: Monitoring Water Levels and Discharges Using Radar Altimetry in an Ungauged River Basin: The Case of the Ogooué, Remote Sensing, 10, https://doi.org/10.3390/rs10020350, 2018.

Bonakdari, H., Larrarte, F., Lassabatere, L., and Joannis, C.: Turbulent velocity profile in fully-developed open channel flows, Environmental Fluid Mechanics, 8, 1–17, https://doi.org/10.1007/s10652-007-9051-6, 2008.

Bonakdari, H., Sheikh, Z., and Tooshmalani, M.: Comparison between Shannon and Tsallis entropies for prediction of shear
545 stress distribution in open channels, Stochastic Environmental Research and Risk Assessment, 29, 1–11, https://doi.org/10.1007/s00477-014-0959-3, 2015.

Briaud, J. L., Chen, H. C., Chang, K. A., Oh, S. J., and Chen, X.: Abutment scour in cohesive materials, NCHRP Report, 24–15(2), Transportation Research Board, National Research Council, Washington, D.C., USA., 2009.

Carniello, L., Defina, A., and D'Alpaos, L.: Modeling sand-mud transport induced by tidal currents and wind waves in shallow
550 microtidal basins: Application to the Venice Lagoon (Italy), Estuarine, Coastal and Shelf Science, 102–103, 105–115, https://doi.org/10.1016/j.ecss.2012.03.016, 2012.

Chahrour, N., Castaings, W., and Barthélemy, E.: Image-based river discharge estimation by merging heterogeneous data with information entropy theory, Flow Measurement and Instrumentation, 81, 102039, https://doi.org/10.1016/j.flowmeasinst.2021.102039, 2021.

555 Chang, W.-Y., Constantinescu, G., Lien, H.-C., Tsai, W.-F., Lai, J.-S., and Loh, C.-H.: Flow Structure around Bridge Piers of Varying Geometrical Complexity, Journal of Hydraulic Engineering, 139, 812–826, https://doi.org/10.1061/(ASCE)HY.1943-7900.0000742, 2013.

Cheng, Z., Koken, M., and Constantinescu, G.: Approximate methodology to account for effects of coherent structures on sediment entrainment in RANS simulations with a movable bed and applications to pier scour, Advances in Water Resources,
560 120, 65–82, https://doi.org/10.1016/j.advwatres.2017.05.019, 2018.

Chiu, C.-L.: Entropy and Probability Concepts in Hydraulics, Journal of Hydraulic Engineering, 113, 583–599, https://doi.org/10.1061/(ASCE)0733-9429(1987)113:5(583), 1987.

Chiu, C.-L.: Entropy and 2-D Velocity Distribution in Open Channels, Journal of Hydraulic Engineering, 114, 738–756, https://doi.org/10.1061/(ASCE)0733-9429(1988)114:7(738), 1988.

565 Chiu, C.-L.: Velocity Distribution in Open Channel Flow, Journal of Hydraulic Engineering, 115, 576–594, https://doi.org/10.1061/(ASCE)0733-9429(1989)115:5(576), 1989.

Chiu, C.-L.: Application of Entropy Concept in Open-Channel Flow Study, Journal of Hydraulic Engineering, 117, 615–628, https://doi.org/10.1061/(ASCE)0733-9429(1991)117:5(615), 1991.

Chiu, C.-L. and Murray, D. W.: Variation of Velocity Distribution along Nonuniform Open-Channel Flow, Journal of
570 Hydraulic Engineering, 118, 989–1001, https://doi.org/10.1061/(ASCE)0733-9429(1992)118:7(989), 1992.

Chiu, C.-L. and Said, C. A. A.: Maximum and Mean Velocities and Entropy in Open-Channel Flow, Journal of Hydraulic Engineering, 121, 26–35, https://doi.org/10.1061/(ASCE)0733-9429(1995)121:1(26), 1995.

Chiu, C.-L., Hsu, S.-M., and Tung, N.-C.: Efficient methods of discharge measurements in rivers and streams based on the probability concept, Hydrological Processes, 19, 3935–3946, https://doi.org/10.1002/hyp.5857, 2005.

575 Constantinescu, G., Koken, M., and Zeng, J.: The structure of turbulent flow in an open channel bend of strong curvature with deformed bed: Insight provided by detached eddy simulation, Water Resources Research, 47, https://doi.org/10.1029/2010WR010114, 2011.

Constantinescu, G., Kashyap, S., Tokyay, T., Rennie, C. D., and Townsend, R. D.: Hydrodynamic processes and sediment erosion mechanisms in an open channel bend of strong curvature with deformed bathymetry, Journal of Geophysical Research:
580 Earth Surface, 118, 480–496, https://doi.org/10.1002/jgrf.20042, 2013.

D'Alpaos, L. and Defina, A.: Mathematical modeling of tidal hydrodynamics in shallow lagoons: A review of open issues and applications to the Venice lagoon, Computers & Geosciences, 33, 476–496, https://doi.org/10.1016/j.cageo.2006.07.009, 2007.

Defina, A.: Two-dimensional shallow flow equations for partially dry areas, Water Resources Research, 36, 3251–3264, https://doi.org/10.1029/2000WR900167, 2000.

585 Defina, A.: Numerical experiments on bar growth, Water Resources Research, 39, 1092, https://doi.org/10.1029/2002WR001455, 2003.

Depetris, P. J.: The Importance of Monitoring River Water Discharge, Frontiers in Water, 3, https://doi.org/10.3389/frwa.2021.745912, 2021.

Di Baldassarre, G. and Montanari, A.: Uncertainty in river discharge observations: a quantitative analysis, Hydrology and
590 Earth System Sciences, 13, 913–921, https://doi.org/10.5194/hess-13-913-2009, 2009.

Dominguez Ruben, L., Szupiany, R. N., Tassi, P., and Vionnet, C. A.: Large meandering bends with high width-to-depth ratios: Insights from hydro-sedimentological processes, Geomorphology, 374, 107521, https://doi.org/10.1016/j.geomorph.2020.107521, 2021.

Dottori, F., Di Baldassarre, G., and Todini, E.: Detailed data is welcome, but with a pinch of salt: Accuracy, precision, and
595 uncertainty in flood inundation modeling, Water Resources Research, 49, 6079–6085, https://doi.org/10.1002/wrcr.20406, 2013.

Ebtehaj, I., Bonakdari, H., Moradi, F., Gharabaghi, B., and Khozani, Z. S.: An integrated framework of Extreme Learning Machines for predicting scour at pile groups in clear water condition, Coastal Engineering, 135, 1–15, https://doi.org/10.1016/j.coastaleng.2017.12.012, 2018.

600 Eltner, A., Sardemann, H., and Grundmann, J.: Technical Note: Flow velocity and discharge measurement in rivers using terrestrial and unmanned-aerial-vehicle imagery, Hydrology and Earth System Sciences, 24, 1429–1445, https://doi.org/10.5194/hess-24-1429-2020, 2020.

Federico, F., Silvagni, G., and Volpi, F.: Scour Vulnerability of River Bridge Piers, Journal of Geotechnical and Geoenvironmental Engineering, 129, 890–899, https://doi.org/10.1061/(ASCE)1090-0241(2003)129:10(890), 2003.

605 Fekete, B. M. and Vörösmarty, C. J.: The current status of global river discharge monitoring and potential new technologies complementing traditional discharge measurements, 309, 129–136, 2002.

Fekete, B. M., Looser, U., Pietroniro, A., and Robarts, R. D.: Rationale for Monitoring Discharge on the Ground, Journal of Hydrometeorology, 13, 1977–1986, https://doi.org/10.1175/JHM-D-11-0126.1, 2012.

Ferro, V.: ADV measurements of velocity distributions in a gravel-bed flume, Earth Surface Processes and Landforms, 28,
610 707–722, https://doi.org/10.1002/esp.467, 2003.

Franca, M. J., Ferreira, R. M. L., and Lemmin, U.: Parameterization of the logarithmic layer of double-averaged streamwise velocity profiles in gravel-bed river flows, Advances in Water Resources, 31, 915–925, https://doi.org/10.1016/j.advwatres.2008.03.001, 2008.

Fujita, I., Watanabe, H., and Tsubaki, R.: Development of a non-intrusive and efficient flow monitoring technique: The space-time image velocimetry (STIV), International Journal of River Basin Management, 5, 105–114, https://doi.org/10.1080/15715124.2007.9635310, 2007.

Fujita, I., Notoya, Y., Tani, K., and Tateguchi, S.: Efficient and accurate estimation of water surface velocity in STIV, Environmental Fluid Mechanics, 19, 1363–1378, https://doi.org/10.1007/s10652-018-9651-3, 2019.

Fulton, J. and Ostrowski, J.: Measuring real-time streamflow using emerging technologies: Radar, hydroacoustics, and the probability concept, Journal of Hydrology, 357, 1–10, https://doi.org/10.1016/j.jhydrol.2008.03.028, 2008.

Giraldo, F. X.: Strong and weak Lagrange-Galerkin spectral element methods for the shallow water equations, Computers & Mathematics with Applications, 45, 97–121, https://doi.org/10.1016/S0898-1221(03)80010-X, 2003.

Gore, J. A. and Banning, J.: Chapter 3 - Discharge Measurements and Streamflow Analysis, in: Methods in Stream Ecology, Volume 1 (Third Edition), edited by: Hauer, F. R. and Lamberti, G. A., Academic Press, Boston, 49–70, https://doi.org/10.1016/B978-0-12-416558-8.00003-2, 2017.

Guo, J.: Modified log-wake-law for smooth rectangular open channel flow, Journal of Hydraulic Research, 52, 121–128, https://doi.org/10.1080/00221686.2013.818584, 2014.

Herschy, R. W.: Streamflow Measurement (3rd ed.), CRC Press, https://doi.org/10.1201/9781482265880, 2009.

Hirt, C. W. and Nichols, B. D.: Volume of fluid (VOF) method for the dynamics of free boundaries, Journal of Computational Physics, 39, 201–225, https://doi.org/10.1016/0021-9991(81)90145-5, 1981.

Horna-Munoz, D. and Constantinescu, G.: A fully 3-D numerical model to predict flood wave propagation and assess efficiency of flood protection measures, Advances in Water Resources, 122, 148–165, https://doi.org/10.1016/j.advwatres.2018.10.014, 2018.

Jodeau, M., Hauet, A., Paquier, A., Le Coz, J., and Dramais, G.: Application and evaluation of LS-PIV technique for the monitoring of river surface velocities in high flow conditions, Flow Measurement and Instrumentation, 19, 117–127, https://doi.org/10.1016/j.flowmeasinst.2007.11.004, 2008.

Kästner, K., Hoitink, A. J. F., Torfs, P. J. J. F., Vermeulen, B., Ningsih, N. S., and Pramulya, M.: Prerequisites for Accurate Monitoring of River Discharge Based on Fixed-Location Velocity Measurements, Water Resources Research, 54, 1058–1076, https://doi.org/10.1002/2017WR020990, 2018.

Khosronejad, A., Kang, S., and Sotiropoulos, F.: Experimental and computational investigation of local scour around bridge piers, Advances in Water Resources, 37, 73–85, https://doi.org/10.1016/j.advwatres.2011.09.013, 2012.

Kirkil, G. and Constantinescu, G.: Effects of cylinder Reynolds number on the turbulent horseshoe vortex system and near wake of a surface-mounted circular cylinder, Physics of Fluids, 27, 075102, https://doi.org/10.1063/1.4923063, 2015.

Kirkil, G., Constantinescu, G., and Ettema, R.: Detached Eddy Simulation Investigation of Turbulence at a Circular Pier with Scour Hole, Journal of Hydraulic Engineering, 135, 888–901, https://doi.org/10.1061/(ASCE)HY.1943-7900.0000101, 2009.

Koken, M., Constantinescu, G., and Blanckaert, K.: Hydrodynamic processes, sediment erosion mechanisms, and Reynolds-number-induced scale effects in an open channel bend of strong curvature with flat bathymetry, Journal of Geophysical Research: Earth Surface, 118, 2308–2324, https://doi.org/10.1002/2013JF002760, 2013.

650 Kundu, S. and Ghoshal, K.: An Entropy Based Model for Velocity-Dip-Position, Journal of Environmental Informatics, 33, 113–128, 2018.

Laursen, E. M.: Scour at Bridge Crossings, Journal of the Hydraulics Division, 86, 39–54, https://doi.org/10.1061/JYCEAJ.0000426, 1960.

Laursen, E. M.: An Analysis of Relief Bridge Scour, Journal of the Hydraulics Division, 89, 93–118, https://doi.org/10.1061/JYCEAJ.0000896, 1963.

655 Lazzarin, T. and Viero, D. P.: Curvature-induced secondary flow in 2D depth-averaged hydro-morphodynamic models: An assessment of different approaches and key factors, Advances in Water Resources, 171, 104355, https://doi.org/10.1016/j.advwatres.2022.104355, 2023.

Lazzarin, T., Defina, A., and Viero, D. P.: Assessing 40 Years of Flood Risk Evolution at the Micro-Scale Using an Innovative Modeling Approach: The Effects of Urbanization and Land Planning, Geosciences, 13, 660 https://doi.org/10.3390/geosciences13040112, 2023a.

Lazzarin, T., Viero, D. P., Defina, A., and Cozzolino, L.: Flow under vertical sluice gates: Flow stability at large gate opening and disambiguation of partial dam-break multiple solutions, Physics of Fluids, 35, 024114, https://doi.org/10.1063/5.0131953, 2023b.

Lazzarin, T., Constantinescu, G., Di Micco, L., Wu, H., Lavignani, F., Lo Brutto, M., Termini, D., and Viero, D. P.: Influence 665 of bed roughness on flow and turbulence structure around a partially-buried, isolated freshwater mussel, Water Resources Research, 59, e2022WR034151, https://doi.org/10.1029/2022WR034151, 2023c.

Lazzarin, T., Chen, A. S., and Viero, D. P.: Beyond flood hazard. Mapping the loss probability of pedestrians to improve risk estimation and communication, Science of The Total Environment, 912, 168718, https://doi.org/10.1016/j.scitotenv.2023.168718, 2024.

670 Le Coz, J., Hauet, A., Pierrefeu, G., Dramais, G., and Camenen, B.: Performance of image-based velocimetry (LSPIV) applied to flash-flood discharge measurements in Mediterranean rivers, Journal of Hydrology, 394, 42–52, https://doi.org/10.1016/j.jhydrol.2010.05.049, 2010.

Li, B. and Zhang, X.: Evolution of outer bank cell in open-channel bends, Environmental Fluid Mechanics, 22, 715–742, https://doi.org/10.1007/s10652-022-09865-2, 2022.

675 Lu, B., Petukhov, V., Zhang, M., Wang, X., Yue, S., Zhou, H., Kholodov, A., and Yu, G.: Prediction of flow-induced local scour depth at the uniform bridge pier using masked attention neural network, Ocean Engineering, 266, 113018, https://doi.org/10.1016/j.oceaneng.2022.113018, 2022.

Luo, H., Fytanidis, D. K., Schmidt, A. R., and García, M. H.: Comparative 1D and 3D numerical investigation of open-channel junction flows and energy losses, Advances in Water Resources, 117, 120–139, 680 https://doi.org/10.1016/j.advwatres.2018.05.012, 2018.

Marini, G. and Fontana, N.: Mean Velocity and Entropy in Wide Channel Flows, Journal of Hydrologic Engineering, 25, 06019009, https://doi.org/10.1061/(ASCE)HE.1943-5584.0001870, 2020.

Martini, P., Carniello, L., and Avanzi, C.: Two dimensional modelling of flood flows and suspended sedimenttransport: the case of the Brenta River, Veneto (Italy), Natural Hazards and Earth System Sciences, 4, 165–181, https://doi.org/10.5194/nhess-4-165-2004, 2004.

Meals, D. W. and Dressing, S. A.: Surface water flow measurement for water quality monitoring projects, 2008.

Mel, R. A., Viero, D. P., Carniello, L., and D'Alpaos, L.: Multipurpose Use of Artificial Channel Networks for Flood Risk Reduction: The Case of the Waterway Padova–Venice (Italy), Water, 12, https://doi.org/10.3390/w12061609, 2020a.

Mel, R. A., Viero, D. P., Carniello, L., and D'Alpaos, L.: Optimal floodgate operation for river flood management: The case study of Padova (Italy), Journal of Hydrology: Regional Studies, 30, 100702, https://doi.org/10.1016/j.ejrh.2020.100702, 2020b.

Moramarco, T. and Singh, V. P.: Formulation of the Entropy Parameter Based on Hydraulic and Geometric Characteristics of River Cross Sections, Journal of Hydrologic Engineering, 15, 852–858, https://doi.org/10.1061/(ASCE)HE.1943-5584.0000255, 2010.

Moramarco, T., Saltalippi, C., and Singh, V. P.: Estimation of Mean Velocity in Natural Channels Based on Chiu's Velocity Distribution Equation, Journal of Hydrologic Engineering, 9, 42–50, https://doi.org/10.1061/(ASCE)1084-0699(2004)9:1(42), 2004.

Moramarco, T., Barbetta, S., and Tarpanelli, A.: From Surface Flow Velocity Measurements to Discharge Assessment by the Entropy Theory, Water, 9, https://doi.org/10.3390/w9020120, 2017.

Moramarco, T., Barbetta, S., Bjerklie, D. M., Fulton, J. W., and Tarpanelli, A.: River Bathymetry Estimate and Discharge Assessment from Remote Sensing, Water Resources Research, 55, 6692–6711, https://doi.org/10.1029/2018WR024220, 2019.

Muste, M., Ho, H.-C., and Kim, D.: Considerations on direct stream flow measurements using video imagery: Outlook and research needs, Journal of Hydro-environment Research, 5, 289–300, https://doi.org/10.1016/j.jher.2010.11.002, 2011.

Muste, M., Hauet, A., Fujita, I., Legout, C., and Ho, H.-C.: Capabilities of Large-scale Particle Image Velocimetry to characterize shallow free-surface flows, Advances in Water Resources, 70, 160–171, https://doi.org/10.1016/j.advwatres.2014.04.004, 2014.

Nezu, I. and Nakagawa, H.: Turbulence in Open Channel Flows, Balkema., Rotterdam, The Netherlands, 1993.

Nikora, V. and Roy, A. G.: Secondary Flows in Rivers: Theoretical Framework, Recent Advances, and Current Challenges, in: Gravel-Bed Rivers, John Wiley & Sons, Ltd, 1–22, https://doi.org/10.1002/9781119952497.ch1, 2011.

Pilbala, A., Riccardi, N., Benistati, N., Modesto, V., Termini, D., Manca, D., Benigni, A., Corradini, C., Lazzarin, T., Moramarco, T., Fraccarollo, L., and Piccolroaz, S.: Real-time biological early-warning system based on freshwater mussels' valvometry data, Hydrology and Earth System Sciences, 28, 2297–2311, https://doi.org/10.5194/hess-28-2297-2024, 2024.

Pivato, M., Carniello, L., Viero, D. P., Soranzo, C., Defina, A., and Silvestri, S.: Remote Sensing for Optimal Estimation of Water Temperature Dynamics in Shallow Tidal Environments, Remote Sensing, 12, https://doi.org/10.3390/rs12010051, 2020.

Proust, S. and Nikora, V. I.: Compound open-channel flows: effects of transverse currents on the flow structure, Journal of Fluid Mechanics, 885, A24, https://doi.org/10.1017/jfm.2019.973, 2020.

van Rijn, L. C.: Equivalent Roughness of Alluvial Bed, Journal of the Hydraulics Division, 108, 1215–1218, https://doi.org/10.1061/JYCEAJ.0005917, 1982.

720 Salaheldin, T. M., Imran, J., and Chaudhry, M. H.: Numerical Modeling of Three-Dimensional Flow Field Around Circular Piers, Journal of Hydraulic Engineering, 130, 91–100, https://doi.org/10.1061/(ASCE)0733-9429(2004)130:2(91), 2004.

Schweitzer, S. A. and Cowen, E. A.: Instantaneous River-Wide Water Surface Velocity Field Measurements at Centimeter Scales Using Infrared Quantitative Image Velocimetry, Water Resources Research, 57, e2020WR029279, https://doi.org/10.1029/2020WR029279, 2021.

Shih, T.-H., Liou, W. W., Shabbir, A., Yang, Z., and Zhu, J.: A new k-ϵ eddy viscosity model for high reynolds number
725 turbulent flows, Computers & Fluids, 24, 227–238, https://doi.org/10.1016/0045-7930(94)00032-T, 1995.

Singh, V. P., Sivakumar, B., and Cui, H.: Tsallis Entropy Theory for Modeling in Water Engineering: A Review, Entropy, 19, https://doi.org/10.3390/e19120641, 2017.

Spada, E., Sinagra, M., Tucciarelli, T., and Biondi, D.: Unsteady State Water Level Analysis for Discharge Hydrograph Estimation in Rivers with Torrential Regime: The Case Study of the February 2016 Flood Event in the Crati River, South Italy,
730 Water, 9, https://doi.org/10.3390/w9040288, 2017.

Sterling, M. and Knight, D.: An attempt at using the entropy approach to predict the transverse distribution of boundary shear stress in open channel flow, Stochastic Environmental Research and Risk Assessment, 16, 127–142, https://doi.org/10.1007/s00477-002-0088-2, 2002.

Sumer, B. M., Christiansen, N., and Fredsøe, J.: The horseshoe vortex and vortex shedding around a vertical wall-mounted
735 cylinder exposed to waves, Journal of Fluid Mechanics, 332, 41–70, https://doi.org/10.1017/S0022112096003898, 1997.

Termini, D. and Moramarco, T.: Application of entropic approach to estimate the mean flow velocity and Manning roughness coefficient in a high-curvature flume, Hydrology Research, 48, 634–645, https://doi.org/10.2166/nh.2016.106, 2017.

Termini, D. and Moramarco, T.: Entropic model application to identify cross-sectional flow effect on velocity distribution in a large amplitude meandering channel, Advances in Water Resources, 143, 103678,
740 https://doi.org/10.1016/j.advwatres.2020.103678, 2020.

Thorne, C. R., Zevenbergen, L. W., Pitlick, J. C., Rais, S., Bradley, J. B., and Julien, P. Y.: Direct measurements of secondary currents in a meandering sand-bed river, Nature, 315, 746–747, https://doi.org/10.1038/315746a0, 1985.

Tognin, D., Finotello, A., D'Alpaos, A., Viero, D. P., Pivato, M., Mel, R. A., Defina, A., Bertuzzo, E., Marani, M., and Carniello, L.: Loss of geomorphic diversity in shallow tidal embayments promoted by storm-surge barriers, Science Advances,
745 8, eabm8446, https://doi.org/10.1126/sciadv.abm8446, 2022.

Vandaele, R., Dance, S. L., and Ojha, V.: Calibrated river-level estimation from river cameras using convolutional neural networks, Environmental Data Science, 2, e11, https://doi.org/10.1017/eds.2023.6, 2023.

Viero, D. P.: Modelling urban floods using a finite element staggered scheme with an anisotropic dual porosity model, Journal of Hydrology, 568, 247–259, https://doi.org/10.1016/j.jhydrol.2018.10.055, 2019.

750 Viero, D. P. and Defina, A.: Water age, exposure time, and local flushing time in semi-enclosed, tidal basins with negligible freshwater inflow, Journal of Marine Systems, 156, 16–29, https://doi.org/10.1016/j.jmarsys.2015.11.006, 2016.

Viero, D. P., D'Alpaos, A., Carniello, L., and Defina, A.: Mathematical modeling of flooding due to river bank failure, Advances in Water Resources, 59, 82–94, https://doi.org/10.1016/j.advwatres.2013.05.011, 2013.

755 Viero, D. P., Peruzzo, P., Carniello, L., and Defina, A.: Integrated mathematical modeling of hydrological and hydrodynamic response to rainfall events in rural lowland catchments, Water Resources Research, 50, 5941–5957, https://doi.org/10.1002/2013WR014293, 2014.

Viero, D. P., Roder, G., Matticchio, B., Defina, A., and Tarolli, P.: Floods, landscape modifications and population dynamics in anthropogenic coastal lowlands: The Polesine (northern Italy) case study, Science of The Total Environment, 651, 1435–1450, https://doi.org/10.1016/j.scitotenv.2018.09.121, 2019.

760 Vyas, J. K., Perumal, M., and Moramarco, T.: Entropy Based River Discharge Estimation Using One-Point Velocity Measurement at 0.6D, Water Resources Research, 57, e2021WR029825, https://doi.org/10.1029/2021WR029825, 2021.

Walters, R. A. and Casulli, V.: A robust, finite element model for hydrostatic surface water flows, Communications in Numerical Methods in Engineering, 14, 931–940, https://doi.org/10.1002/(SICI)1099-0887(1998100)14:10<931::AID-CNM199>3.0.CO;2-X, 1998.

765 Yang, S.-Q., Tan, S.-K., and Lim, S.-Y.: Velocity Distribution and Dip-Phenomenon in Smooth Uniform Open Channel Flows, Journal of Hydraulic Engineering, 130, 1179–1186, https://doi.org/10.1061/(ASCE)0733-9429(2004)130:12(1179), 2004.

Yang, S.-Q., Tan, S. K., and Wang, X.-K.: Mechanism of secondary currents in open channel flows, Journal of Geophysical Research: Earth Surface, 117, https://doi.org/10.1029/2012JF002510, 2012.

Yang, Y., Xiong, X., Melville, B. W., and Sturm, T. W.: Flow Redistribution at Bridge Contractions in Compound Channel 770 for Extreme Hydrological Events and Implications for Sediment Scour, Journal of Hydraulic Engineering, 147, 04021005, https://doi.org/10.1061/(ASCE)HY.1943-7900.0001861, 2021.

Yoshimura, H. and Fujita, I.: Investigation of free-surface dynamics in an open-channel flow, Journal of Hydraulic Research, 58, 231–247, https://doi.org/10.1080/00221686.2018.1561531, 2020.

Zhang, Z., Zhou, Y., Liu, H., and Gao, H.: In-situ water level measurement using NIR-imaging video camera, Flow 775 Measurement and Instrumentation, 67, 95–106, https://doi.org/10.1016/j.flowmeasinst.2019.04.004, 2019.